

# Periodic orbits of neutral test particles in Reissner-Nordström naked singularities

Zoe C S Chan<sup>1\*</sup> and Yen-Kheng Lim<sup>2</sup>

<sup>1,2</sup>*Department of Physics, Xiamen University Malaysia, 43900 Sepang,  
Malaysia.*

\*Corresponding author(s). E-mail(s): [bravychancs@gmail.com](mailto:bravychancs@gmail.com);  
Contributing authors: [yenkheng.lim@gmail.com](mailto:yenkheng.lim@gmail.com),  
[yenkheng.lim@xmu.edu.my](mailto:yenkheng.lim@xmu.edu.my);

## Abstract

We conduct studies on Levin's taxonomy of periodic orbits for neutral test particles around a Reissner-Nordström naked singularity. It was known that naked singularities could harbor two distinct regions of time-like bound orbits and thus we expect periodic orbits to appear in both regions. It is possible for a pair of periodic orbits from both regions to possess the exact same angular momentum  $L$  and energy  $E$  values. We chart the sets of periodic orbits in  $(L, E)$ -parameter space and highlight the general distribution pattern of these sets for three possible scenarios. Regions within  $(L, E)$ -space can be partitioned into multiple domains  $\mathcal{D}_k$  based on the roots configuration of the quartic polynomial  $P(u)$  where  $u$  is the inverse radial coordinate. Consequently, each domain and interestingly enough, portions of certain periodic orbits sets that lie in different  $\mathcal{D}_k$  require different analytical solutions to plot the resulting orbit. Furthermore, we uncover physical properties of some hypothetical circular orbits residing in the inner region from analysing the  $(L, E)$ -space.

**Keywords:** Periodic Orbits, Naked Singularity, Reissner-Nordström, Jacobian Elliptic Functions

## 1 Introduction

The Reissner-Nordström (RN) metric is an exact solution to Einstein-Maxwell field equations which describe a static, asymptotically flat spacetime outside a charged, non-rotating, spherically symmetric compact body of mass  $M$ . It was determined

independently by Reissner [1] in 1916 and Nordström [2] in 1918. This solution was generally deemed unrealistic since the compact body is unlikely able to acquire a relatively large charge-to-mass ratio  $Q/M$ . This was exemplified by Zajaček et. al. [3] where they find constraints of the Milky Way’s central black hole (Sgr A\*) charge to be  $Q/M \simeq 0$ . Nevertheless, studying the geodesics of test particles in the vicinity of a charged compact body are still important in relativistic astrophysics as they provide approximate models to astrophysical processes such as gravitational waves detection [4, 5] or direct imaging of black holes shadows [6–8].

Earlier, Levin et.al. classified the anatomy of periodic, zoom-whirl orbits [9] in a series of papers [10–18]. These periodic orbits were indexed by three non-negative integers  $(z, w, v)$  based on the geometric and topological features of the orbits structure.  $z$  counts the number of ellipses in an orbit,  $w$  is the number of near-center whirls and  $v$  is the order in which the ellipses are traced out. Then, every periodic orbits can be parametrized by a dimensionless rational number  $q$ , given by  $q = w + \frac{v}{z}$ . If  $q$  is irrational, it corresponds to a quasiperiodic orbit. Initially, the taxonomy was meant to aid calculations in gravitational-waves detection, specifically for extreme mass ratio inspirals that exhibit zoom-whirl behaviour. Lately, these periodic orbits descriptions were applied to other theoretical spacetime settings or alternate gravity theories. [19–28].

Naked singularities are hypothetical singularities where there is no event horizon surrounding the singularity, so any distant observer could observe the singularity in principle. For RN case, this occurs when the compact body’s charge exceeds its mass, i.e.  $Q/M > 1$ . Penrose conjectured that naked singularities are impossible to observe in nature and must always be hidden behind an event horizon via his infamous cosmic censorship hypothesis [29]. On the flip side, there is an ongoing trend to detect the existence of naked singularities based on its exotic property of allowing multiple regions of bound orbits [30–34]. Some newly proposed naked singularity kinds such as sub-solar mass [35] or primordial [36] have been put forward too.

Recently, one of the authors contribute more theoretical descriptions to Levin’s taxonomy for Schwarzschild spacetime [37]. Several analytical solutions were parametrized in terms of parameters characterizing the geometry of an ellipse, the eccentricity  $e$  and latus rectum  $\lambda$ . This enable the complete interpolation of  $q$ -distribution of sets containing values of the conserved quantities  $L$  and  $E$  for  $0 \leq e < 1$ . Each of these sets appear as a ‘branch’ emanating from the stable circular orbit segment (which acts as the zero-eccentricity limit). These  $q$ -branches distribute as a discrete line spectrum, resembling the emission spectrum of chemical elements. An advantage of performing analysis from the  $(L, E)$ -parameter space is that it uncover features of certain types of orbits that may not be present in other graphs.

Gathering the motivations mentioned above, for this paper, we will like to extend the works of [37] by considering only neutral time-like test particles orbiting a Reissner-Nordström naked singularity. For black holes, time-like circular orbits were proven to exist only in a single region outside the event horizon [17, 31, 38]. So, the circular orbits curves of RN black holes have similar structures as the Schwarzschild case. The main difference is that larger black holes charge decrease the lower bound of circular orbits radius and in return, increase the range of  $L$  and  $E$  values. Accordingly, the circular

orbits curve of RN black holes with larger  $Q/M$  shift towards the  $L$  and  $E$ -axes in  $(L, E)$ -space.

Key results for circular orbits of RN naked singularity by Pugliese et.al. [38] show that for a small range of  $Q/M$ , there exist a second smaller region that allow time-like stable circular orbits. As such, we expect the circular orbits curve in  $(L, E)$ -space to have another segment representing the stable circular orbits of this smaller region and thus, new sets of  $q$ -branches could be distributed along this segment. There are also three distinct scenarios for naked singularity circular orbits. Each scenario occur in the following charge range:  $M < Q < \sqrt{\frac{9}{8}} M$ ,  $\sqrt{\frac{9}{8}} M \leq Q < \frac{\sqrt{5}}{2} M$  and  $Q \geq \frac{\sqrt{5}}{2} M$ . From here on, we will refer to these scenarios, in order, as Case 1, 2 and 3.

The rest of the paper is organized as follows. In Sec. 2, we derive the relevant equations of motion from the RN metric and also review key techniques from [37] to chart the periodic orbits distribution in  $(L, E)$ -space. In Sec. 3, we relate how the roots configuration of the quartic polynomial  $P(u)$  at different points in  $(L, E)$ -space determine the orbit types and then show which analytical solution in terms of  $P(u)$  roots to use at each point. Sec. 4 generalize the domains in  $(L, E)$ -space where we can locate periodic orbits and highlight  $q$ -branch distribution pattern for all three naked singularity scenarios.

We inform the readers that we work in Lorentzian metric signature  $(-, +, +, +)$  alongside geometrized units  $c = G = 1$ . We adopt the extended periodic orbit taxonomy notation,  $(z, w, v; e)$  introduced in [37] and notations of some special kinds of circular orbits from [38]. We generally colored the text and labels in the figures as **blue** to represent periodic orbits residing in the outer region and **red** for the inner ones. All numerical values in the figures are displayed up to 5 significant figures unless stated otherwise.

## 2 Equations of motions and the $(L, E)$ parameter space

Here, we review the derivation of the geodesics for neutral test particle via Lagrangian formalism in Sec. 2.1. In Sec. 2.2, we show how the analytical expressions for the particle's conserved energy  $E$  and angular momenta  $L$  in terms of circular orbits radius  $r_c$  and geometric parameters  $e$  and  $\lambda$  describe periodic orbits graphically on  $(L, E)$ -parameter space. Derivation of  $e, \lambda$  parametric expressions is given in Appendix A. In Sec. 2.3, we review techniques from [37] for determining  $\lambda$  numerically while fixing every other parameters  $Q, e, z, w$  and  $v$  via the relation between  $P(u)$  and the elliptic integral. This enable us to map the whole distribution of periodic orbits on  $(L, E)$ -space, taking a RN black hole as an example.

### 2.1 Geodesics from Lagrangian formalism

The Reissner-Nordström spacetime is described by the metric line element and horizon function

$$ds^2 = -f(r) dt^2 + f^{-1}(r) dr^2 + r^2 (d\theta^2 + \sin^2 \theta d\phi^2), \quad (1a)$$

$$f(r) = 1 - \frac{2M}{r} + \frac{Q^2}{r^2}, \quad (1b)$$

with associated electromagnetic gauge potential and field

$$A = \frac{Q}{r} dt, \quad F = dA = -\frac{Q}{r^2} dt \wedge dr, \quad (2)$$

The central body is a black hole if  $0 \leq Q \leq M$  with horizons at  $r_{\pm} = M \pm \sqrt{M^2 - Q^2}$  and is a horizonless naked singularity if  $Q > M$ . Geodesics of neutral time-like particles are described by the parametrised curve  $x^{\mu}(\tau)$ , where  $\tau$  is the proper time parameter. The test particle's Lagrangian  $\mathcal{L}(x, \dot{x}) = \frac{1}{2} g_{\mu\nu} \dot{x}^{\mu} \dot{x}^{\nu}$  is explicitly

$$\mathcal{L} = \frac{1}{2} \left( -f \dot{t}^2 + f^{-1} \dot{r}^2 + r^2 \dot{\theta}^2 + r^2 \sin^2 \theta \dot{\phi}^2 \right), \quad (3)$$

where over-dots denote derivatives with respect to  $\tau$ .

The canonical momenta are  $p_{\mu} = \frac{\partial \mathcal{L}}{\partial \dot{x}^{\mu}}$ . The isometries of spacetime are generated by the Killing vector fields  $\xi = \xi^{\mu} \partial_{\mu}$ , that are associated with quantities conserved throughout the geodesics. In this case,  $\partial_t$  and  $\partial_{\phi}$  are the Killing vectors and their corresponding momenta  $p_t$  and  $p_{\phi}$  are conserved. Referring to components of the Lagrangian (3), the constants of motion associated with these fields are

$$E \equiv -\xi^t p_t = f \dot{t}, \quad L \equiv \xi^{\phi} p_{\phi} = r^2 \sin^2 \theta \dot{\phi}, \quad (4)$$

where  $E$  and  $L$  are the energy and angular momentum of the test particle respectively. Then, we can represent two first integrals in terms of these conserved quantities. Rearranging Eqs.(4) gives<sup>1</sup>

$$\dot{t} = \frac{E}{f}, \quad \dot{\phi} = \frac{L}{r^2 \sin^2 \theta} \quad (5)$$

The normalization condition for time-like particles gives another first integral,

$$g_{\mu\nu} \dot{x}^{\mu} \dot{x}^{\nu} = -1, \quad (6)$$

rearranging Eq.(1a) and doing relevant substitutions with Eqs.(5) leads to

$$\dot{r}^2 + r^2 f \dot{\theta}^2 = E^2 - \left( 1 + \frac{L^2}{r^2 \sin^2 \theta} \right) f \quad (7)$$

Due to the geometry being spherically symmetric, we can restrict all trajectories to lie on the equatorial plane  $\theta = \frac{\pi}{2}$ , without loss of generality. In the end, the essential

---

<sup>1</sup>Notice these first integrals are similar to the Schwarzschild ones, with only the metric function  $f$  having an additional  $\frac{Q^2}{r^2}$  term. An alternative formalism using Hamilton-Jacobi equations can be found in Ref.[37].

equations are the energy equation upon rearranging Eq.(7),

$$\dot{r}^2 + V_{\text{eff}} = E^2, \quad (8a)$$

$$V_{\text{eff}} = \left(1 + \frac{L^2}{r^2}\right) \left(1 - \frac{2M}{r} + \frac{Q^2}{r^2}\right), \quad (8b)$$

and the quartic radial polynomial from taking  $\frac{\dot{r}}{\dot{\phi}} = \frac{dr}{d\phi}$ . As in classical central force problems, we change the variable of this differential equation to the inverse radial coordinate  $u = \frac{1}{r}$ , giving us the  $P(u)$  polynomial which can be written out in two forms,

$$\frac{du}{d\phi} = \pm \sqrt{P(u)}, \quad (9a)$$

$$P(u) = -Q^2 u^4 + 2Mu^3 - \left(1 + \frac{Q^2}{L^2}\right) u^2 + \frac{2M}{L^2} u - \frac{1 - E^2}{L^2} \quad (9b)$$

$$\equiv Q^2(a - u)(b - u)(c - u)(u - d), \quad (9c)$$

where  $a, b, c, d$  are the roots of  $P(u)$  that could take on real or complex values.

In essence,  $P(u)$  determines the geometry of orbits from its roots disposition where each root represent the turning point ( $\dot{r} = 0$ ) of the orbit [39]. This also correlate with the number of bound orbits that can exist in a given spacetime. From the presence of the square root in (9a), it is clear that physically allowed solutions only occur for  $P(u) \geq 0$ . We will explain more on  $P(u)$  and its applications in later sections.

## 2.2 Solutions in terms of circular orbits and $e, \lambda$ parameters

In the context of the periodic orbits taxonomy [10, 37], circular orbits were identified to be the zero-eccentricity limit. Expressions of  $L$  and  $E$  in terms of the circular orbits radius  $r_c$  for neutral test particle in RN spacetime have appeared in the literature [17, 38]. A detailed derivation method can be found in Ref.[17]. Basically, the conditions to obtain circular orbits are  $\dot{r} = 0$  and  $V'_{\text{eff}} = 0$ . The expressions are given by,

$$L(r_c, Q) = \frac{r_c \sqrt{Mr_c - Q^2}}{\sqrt{r_c^2 - 3Mr_c + 2Q^2}}, \quad E(r_c, Q) = \frac{r_c^2 - 2Mr_c + Q^2}{r_c \sqrt{r_c^2 - 3Mr_c + 2Q^2}} \quad (10)$$

Then, we can map the set of  $r_c$  values with Eqs.(10) for some fix  $Q$  in  $(L, E)$ -space. An additional condition  $V''_{\text{eff}}$  checks the stability of orbits of each segment of the curve (Fig.1). Orbits are stable if this second derivative is positive and unstable if negative.  $V''_{\text{eff}} = 0$  occur at the critical points, which can be interpreted as the point where the set of  $r_c$  values change stability upon crossing it. The critical point is normally comprise of the *innermost stable circular orbit* (ISCO) but a second one, sometimes referred to as the *outermost stable circular orbit* (OSCO) [40, 41] of the inner region appear in Case 1 and 2 naked singularity (Fig.2).

Geometrical bound and unbound orbits are related to the eccentricity  $e$  of a conic section. Bound orbits have  $0 \leq e < 1$ , resulting in the orbits having circular or elliptic-like shapes whereas  $e \geq 1$  describes unbound orbits that are hyperbolic trajectories. Periodic orbits are trajectories that return exactly to its initial condition after a fixed orbital period and some finite amount of precession. Thus, all periodic orbits must be bound geometrically. The non-relativistic limit occurs at  $r_c \rightarrow \infty$ . On the unstable circular orbit segment,  $r_c$  approach the other limit, the photon sphere at  $r_{\gamma+}$  as both  $L$  and  $E$  diverge (Fig.1).

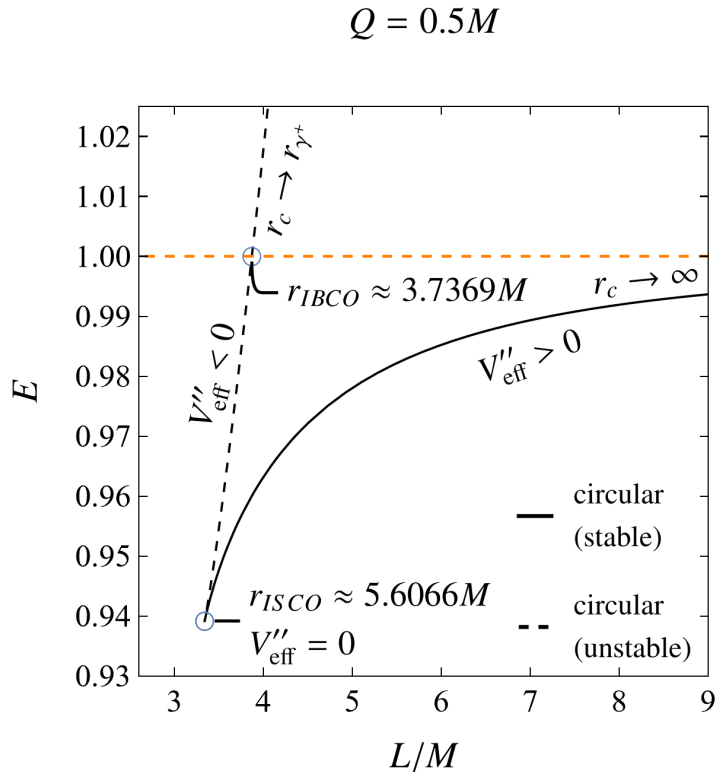


**Fig. 1** A time-like circular orbits parametric curve for RN black holes in  $(L, E)$ -space. The orange dashed line at  $E = 1$  acts as the separator between regions containing orbits that are energetically bound region ( $E < 1$ ) and unbound ( $E \geq 1$ ).

Now, we summarize key features of some special types of circular orbits that are exclusive to naked singularity as covered in [38].  $r_{\gamma-}$  represent the null circular orbit in the inner region and is stable unlike the outer counterpart. Time-like circular orbits are forbidden within the range  $r_{\gamma-} \leq r_c \leq r_{\gamma+}$ . Both null circular orbits only appear in Case 1 since both of their radii merge at  $r = 1.5M$  when  $Q = \sqrt{\frac{9}{8}}M$ .  $r_*$  is the radius of the smallest possible time-like circular orbit surrounding a naked singularity where particles possess zero angular momentum and appear static to distant observers.

Alternatively, we could describe  $r_*$  as the spherical interface between the gravitational attraction region  $r > r_*$  and the repulsive ‘anti-gravity’ region  $r < r_*$ . [38, 42] gave justifications on how  $r_*$  exists.

There are also  $r_c$  values located exactly on the  $E = 1$  line in  $(L, E)$ -space (see Fig.1 and 2). These act like transition points between energetically bound ( $E < 1$ ) and energetically unbound ( $E \geq 1$ ) circular orbits. The one at the unstable  $r_c$  segment is normally known as the *innermost bound circular orbit* (IBCO), although it is technically an energetically unbound circular orbit already. For Cases 1 and 2 naked singularity, there is another  $E = 1$  point at the inner stable  $r_c$  segment which we shall label it as the *innermost unbound circular orbit* (IUCO)<sup>2</sup>. It is indeed the smallest possible energetically unbound circular orbit and also contain information of the innermost distance a hyperbolic trajectory could reach in a naked singularity background.

On a side note, the singular point of the curves where different stability segments meet are known as *cusps* (Figs.1, 2). The usual way of deriving the rather long analytical solution for critical points involve solving the conditions  $\dot{r} = 0$ ,  $V'_{\text{eff}} = 0$  and  $V''_{\text{eff}} = 0$  together [17, 38]. However, in our case, we can use the fact that the cusp is also a point on the circular orbits parametric curve where the first derivative with respect to  $r_c$  of both Eqs.(10) are zero. So we could easily get the numerical value of critical points by solving

$$\frac{\partial}{\partial r_c} L(r_c, Q) = 0 \quad \text{or} \quad \frac{\partial}{\partial r_c} E(r_c, Q) = 0 \quad (11)$$

There will be three solutions as  $V''_{\text{eff}} = 0$  yields a cubic equation. For black holes, the only real solution correspond to the ISCO. For naked singularities, there are three real solutions where ISCO is the largest solution, the Case 2 OSCO is the middle value and the smallest solution is unphysical since it lie in  $r_c < r_*$ . Alternatively, analytical expressions for the critical points are provided in Appendix B; (B2) for the ISCO and (B1) for the OSCO. Case 2 can be subdivided into two variations where Case 2A and Case 2B fall in  $Q \in [\sqrt{9/8} M, 1.0887M]$  and  $Q \in (1.0887M, \sqrt{5/2}M)$  respectively. We obtain the maximum charge  $Q \approx 1.0887M$  for Case 2A by solving the conditions  $E(r_c, Q) = 1$  (10) and  $\frac{\partial}{\partial r_c} E(r_c, Q) = 0$ . In Case 3, the two critical points coalesce at  $r = 2.5M$  of  $Q = \frac{\sqrt{5}}{2} M$  and thereby, only a single region of stable bound orbits remain.

To see the full picture of periodic orbits map in  $(L, E)$ -space, we still need expressions in terms of  $e$  and  $\lambda$ . This can be done by first reparametrizing the  $u$ -roots with these parameters [37, 39]. Refer to Appendix A for derivation guide. We label the four roots of  $P(u)$  as

$$a = \frac{-(Q^2 - M\lambda)^2 - H(Q, e, \lambda)}{Q^2\lambda(Q^2 - M\lambda)}, \quad b = \frac{-(Q^2 - M\lambda)^2 + H(Q, e, \lambda)}{Q^2\lambda(Q^2 - M\lambda)}, \quad (12a)$$

---

<sup>2</sup>Sec. 3.3 explains the role and naming convention of this circular orbits better when we get into root configuration analysis.

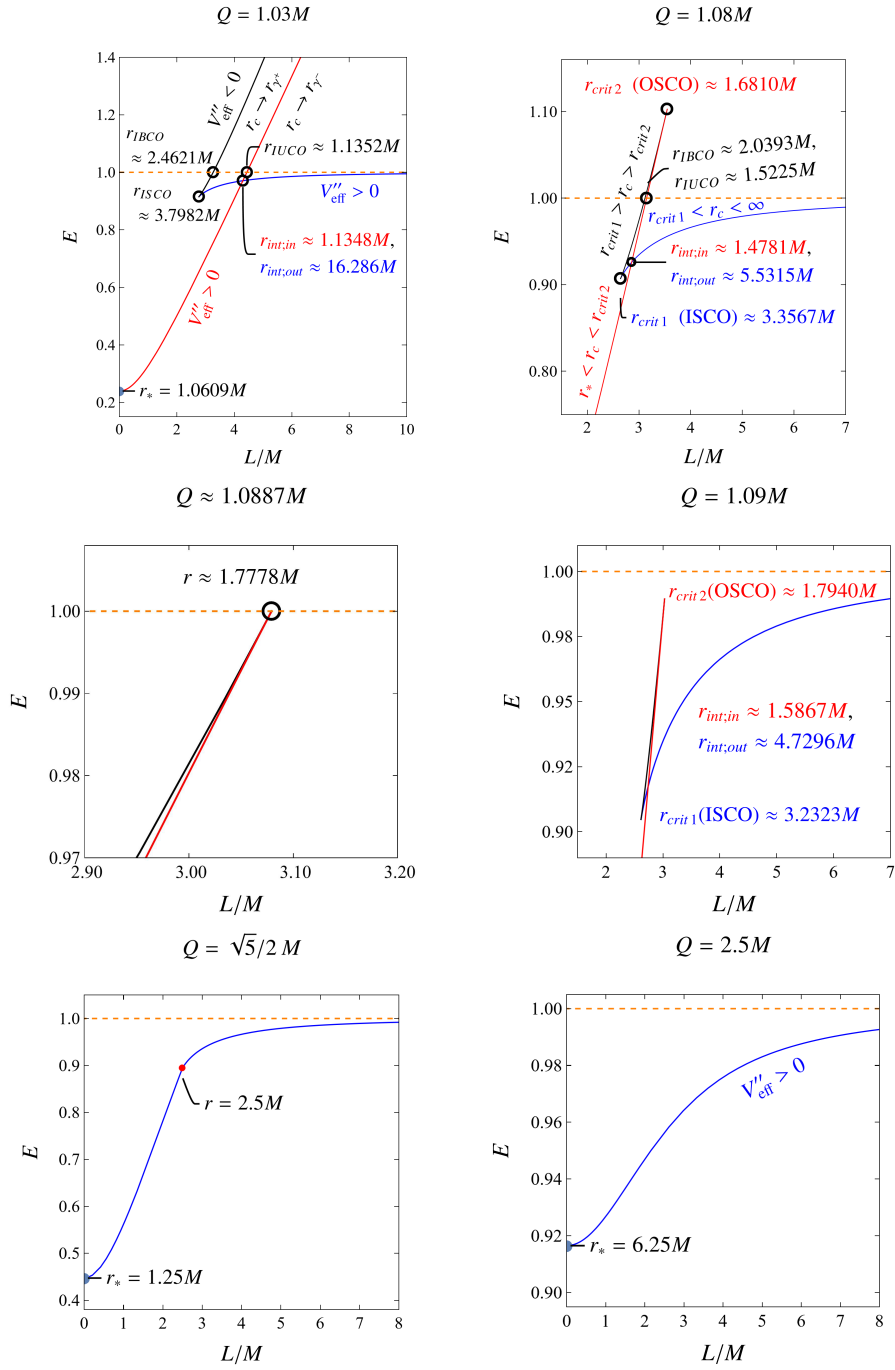


**Fig. 2** The evolution of circular orbits curves for naked singularities from Case 1 (top left) to Case 2A (top right and center left), Case 2B (center right) and finally Case 3 in the bottom row.



$$c = \frac{1+e}{\lambda}, \quad d = \frac{1-e}{\lambda}, \quad (12b)$$

$$H(Q, e, \lambda) = \sqrt{(Q^2 - M\lambda)(e^2 Q^6 + M\lambda(Q^4 - M^2\lambda^2 + Q^2\lambda(\lambda - M)))} \quad (12c)$$

As in [37, 39], the roots  $c$  and  $d$  represent the  $u$ -value of the periastron  $u_p$  and the apastron  $u_a$  of the orbits respectively and always take real values.  $e$  and  $\lambda$  can be easily checked with [13],

$$e = \frac{u_p - u_a}{u_p + u_a}, \quad \lambda = \frac{2}{u_p + u_a} \quad (13)$$

The  $a, b$  pair (12a) is a consequence from the polynomial being quartic and have no analogue in Schwarzschild metric (or any spacetime with a degree 3 radial polynomial). This pair could take complex values due to the presence of the square root function  $H(Q, e, \lambda)$  (12c). The reparametrized  $L, E$  expressions are

$$L(e, \lambda, Q) = \sqrt{\frac{(M\lambda^3 - Q^2\lambda^2)}{g(e, \lambda, Q)}}, \quad E(e, \lambda, Q) = \sqrt{\frac{f(e, \lambda, Q)}{\lambda^2 g(e, \lambda, Q)}}, \quad (14a)$$

$$f(e, \lambda, Q) = \lambda^4 - 4M\lambda^3 + (2(e^2 + 1)Q^2 - 4(e^2 - 1)M^2)\lambda^2 + 4(e^2 - 1)MQ^2\lambda + (e^2 - 1)^2Q^4, \quad (14b)$$

$$g(e, \lambda, Q) = \lambda^2 - (e^2 + 3)M\lambda + 2(e^2 + 1)Q^2 \quad (14c)$$

Eqs.(14a) allow us to interpolate curves that encode the set of periodic orbits ( $L, E$ ) values for any  $q$  within  $0 \leq e < 1$ . Visually, we observe these curves emanating as ‘branches’ from the stable  $r_c$  segments which are the  $e = 0$  limit and hence why we refer to them as  $q$ -branches (see Figs.3 and 4). The upper limit of  $e$  for any  $q$ -branch is clearly  $e = 1$  since this represent the parabola, a type of hyperbolic trajectory.

### 2.3 Black holes $q$ -branch distribution in ( $L, E$ )-space

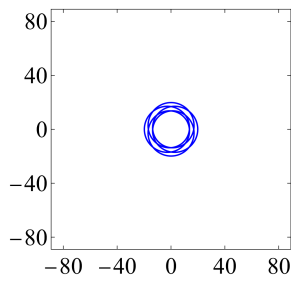
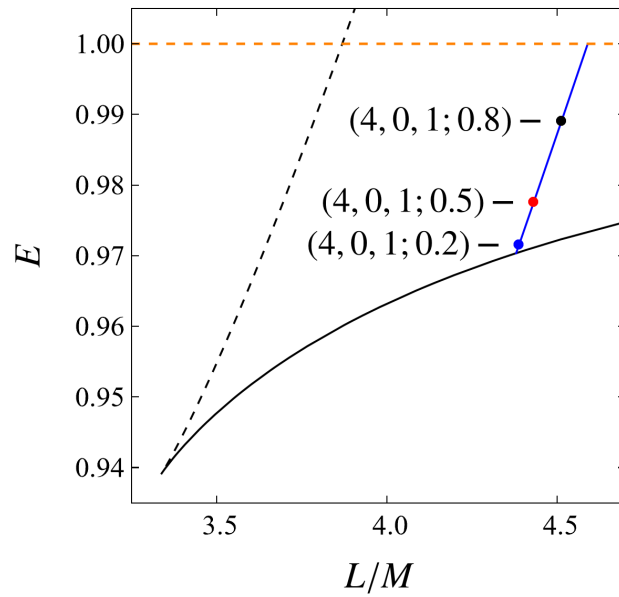
Now, we will show the procedures that allow us to chart out the entire rational  $q$ -branch distribution for different configurations of  $z, w, v$  and  $Q$ . With the  $r_c$  parameter, we can derive an equation that compute the discrete sets of the  $q$ -branches *emanation points* from the stable circular orbits segments. First, we obtain the the second-order differential equation in  $r$  from solving the Euler-Lagrange equation  $\frac{d}{d\tau} \frac{\partial \mathcal{L}}{\partial \dot{r}} = \frac{\partial \mathcal{L}}{\partial r}$  of (3),

$$\ddot{r} = \frac{f' \dot{r}^2}{2f} - \frac{f' E^2}{2f} + \frac{L^2 f}{r^3} \quad (15)$$

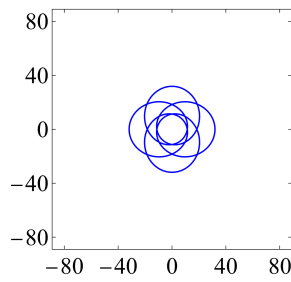
Then, we linearize Eq.(15) in the vicinity of  $r_c$  by small perturbation approach,

$$r(\tau) = r_c + \varepsilon \delta r(\tau), \quad (16)$$

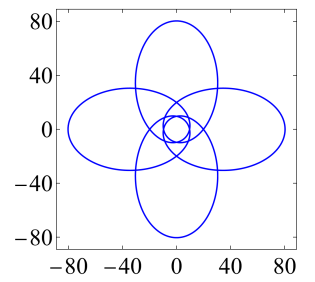
$$Q = 0.5M$$



• (4, 0, 1; 0.2)



• (4, 0, 1; 0.5)



• (4, 0, 1; 0.8)

**Fig. 3** Top figure: The interpolated blue solid line is the  $q$ -branch containing the set of  $(L, E)$  values of the  $(4, 0, 1; e)$  orbit for  $e = 0.2$ ,  $e = 0.5$  and  $e = 0.8$ .

Substituting Eqs.(10) and (16) into Eq.(15), up to linear order in  $\varepsilon$ , we get

$$\delta\ddot{r} = -\Omega^2\delta r, \quad \Omega = \frac{1}{r_c^2} \sqrt{\frac{Mr_c^3 - 6Mr_c^2 + 9MQ^2r_c - 4Q^4}{r_c^2 - 3Mr_c + 2Q^2}} \quad (17)$$

Choosing suitable initial conditions [37], we relate the particle's  $\phi$  increment to its orbital period given by  $\tau = \frac{2\pi}{\Omega}$  and the  $q$ -parameter [10],

$$q + 1 = \frac{\Delta\phi}{2\pi} \simeq \frac{L_c}{r_c^2\Omega} = r_c \sqrt{\frac{Mr_c - Q^2}{Mr_c^3 - 6Mr_c^2 + 9MQ^2r_c - 4Q^4}} \quad (18)$$

Then rearrange Eq.(18) to obtain a cubic equation in  $r_c$ ,

$$M((q+1)^2 - 1)r_c^3 + (Q^2 - 6M^2(q+1)^2)r_c^2 + 9MQ^2(q+1)^2r_c - 4Q^4(q+1)^2 = 0 \quad (19)$$

The emanation points are the solutions of Eq.(19). Similar to (11), there are three real  $r_c$  solutions for  $Q > M$ . For Case 1 and 2, we take the larger two solutions and ignore the smallest solution whose value is always less than  $r_*$ . But for Case 3, we only need the smallest solution instead since that is the only  $r_c$  value where the  $q$ -branches could emanate from continuously for  $e \simeq 0$ . We will remind the readers of these choices again in later sections.

Coming back to the  $P(u)$  polynomial, we will first separate the differential equation (9a) and then take the integrals on both sides. This gives the general form of an *elliptic integral*,

$$\phi(u) = \int_{u_1}^u \frac{du}{\sqrt{P(u)}} \quad (20)$$

with  $u_1$  as the initial condition. As taught in [43, 44], by algebraic reduction, the polynomial  $P(u)$  can be written in its factored form (9c). Furthermore, (20) can be expressed in the Jacobi form of the first kind, that is  $gF(\psi, k)$  where  $g$  is a constant,  $\psi$  is the amplitude and  $k$  is the elliptic modulus which could be complex. The function  $F$  is the incomplete elliptic integral of the first kind. Values of  $g, \psi$  and  $k$  are dependant on the roots  $a, b, c, d$  (12).

We have two usages for this elliptic integral. Here, we use it to set up the relation to determine  $\lambda$  numerically for any fixed  $(z, w, v; e)$  sets. This enable us to chart  $(L, E)$  values for any  $e > 0$  to complement with Eq.(19). Following the procedure in Ref.[37], we choose the initial condition to be at the apastron  $d$  and roots ordering  $a > b > c \geq u > d$ , as given in 252.00, pg.103 [43],

$$\begin{aligned} \phi(u) &= \int_d^u \frac{du}{\sqrt{Q^2(a-u)(b-u)(c-u)(u-d)}} \\ &= \frac{2}{Q\sqrt{(a-c)(b-d)}} F \left( \arcsin \sqrt{\frac{(a-c)(u-d)}{(c-d)(a-u)}}, \sqrt{\frac{(a-b)(c-d)}{(a-c)(b-d)}} \right), \end{aligned} \quad (21)$$

where,  $g = \frac{2}{Q\sqrt{(a-c)(b-d)}}$ ,  $\psi = \arcsin \sqrt{\frac{(a-c)(u-d)}{(c-d)(a-u)}}$  and  $k^2 = \frac{(a-b)(c-d)}{(a-c)(b-d)}$ .

Then, the accumulated angle  $\Delta\phi_r$  between successive periastrons per orbital period is

$$\Delta\phi_r = 2\phi(u_p) = 2\phi(c) = gF\left(\frac{\pi}{2}, k\right) = gK(k), \quad (22)$$

where  $K(k)$  is the complete elliptic integral of the first kind. Relating it with  $q$  again,

$$\frac{\Delta\phi_r}{2\pi} = \frac{gK(k)}{2\pi} = q + 1 = w + \frac{v}{z} + 1, \quad (23)$$

then substitute Eqs.(12) first into (21) then (23). Upon rearrangement, we have

$$\frac{\pi}{2} \sqrt{\frac{J(Q, e, \lambda)}{(M\lambda^3 - Q^2\lambda^2)}} \left( w + \frac{v}{z} + 1 \right) = K \left( \sqrt{\frac{4eH(Q, e, \lambda)}{J(Q, e, \lambda)}} \right) \quad (24)$$

where  $J(Q, e, \lambda) = 2eH(Q, e, \lambda) + M\lambda^3 - 6M^2\lambda^2 - (e^2 - 9)MQ^2\lambda + 2(e^2 - 2)Q^4$  and  $H(Q, e, \lambda)$  is as given in (12c). Eq.(24) coupled with relevant solutions of Eq.(19) reveal the complete distribution of periodic orbits for any fixed  $Q$ . It can be tricky to find the right  $\lambda$ , especially for periodic orbits from the inner region since the polynomials in (23) typically yield multiple real solutions. Our practice is to take the closest monotonically increasing  $(e, \lambda)$  values starting from  $e = 0$  and avoid nonsensical large jumps between values. Subsequently, it is checked that the solutions return rational  $q$  and produce plots of orbits that closes on itself.

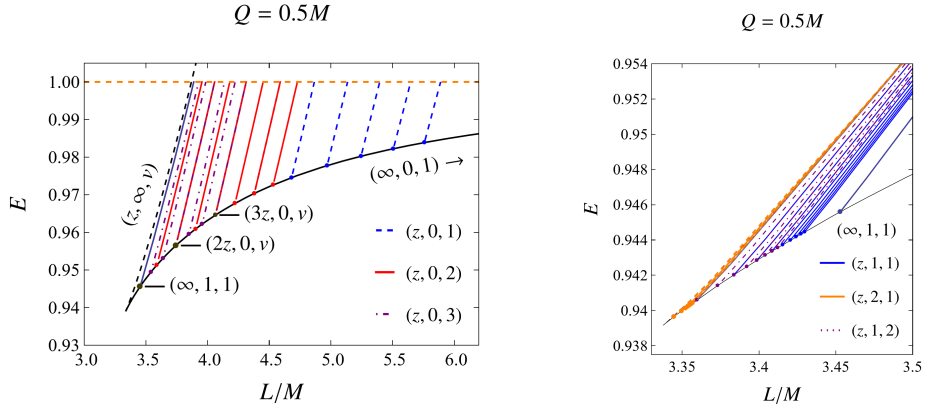


**Fig. 4** The  $q$ -branch general distribution for RN black holes with  $0 \leq Q \leq M$ . Dots on the stable  $\tau_c$  segment are the emanation points. Here,  $z$  values are from 1 to 9.

The general  $q$ -branch distribution pattern for black holes in  $(L, E)$ -space was first discovered in [37] for the Schwarzschild ( $Q = 0$ ) case. To summarize the distribution pattern, the sequence of branch of increasing  $z$  always goes from left to right whereas sequence of increasing  $v$  shift all branches of fixed  $z, w$  to the left. Increasing  $w$  drastically shrink the range of  $L$  values and visually, all  $w \geq 2$  sequences are indistinguishable from one another (Fig.4).

Because of the coprime condition of  $z$  and  $v$  [10], increasing unit value of  $v$  require removing all integers of  $z \leq v$ . Taking an example, if the largest  $z$  value is 9 and  $v$  is 2, then the smallest  $z$  value must be 3. We certainly notice that branches where  $z$

and  $v$  are not coprime all emanate from the same  $r_c$  point and completely overlap one another, like the  $(2, 0, 1) - (4, 0, 2) - (6, 0, 3)$  triplets in Fig.4

The limit branches are also important, especially when dealing with domains in  $(L, E)$ -space involving complex  $u$ -roots later on. As before, increasing  $w$  cause the  $(z, w, v)$  sets to converge towards the unstable circular orbit segment. Thus, the unstable circular orbits segment is equivalent to the  $w = \infty$  branch and is the overall left-most boundary of the distribution [37].  $w = 0$  are the right boundary for  $w$  sub-divisions. By the coprime condition again, the  $(z, w, 1)$  and  $(z, w, v)$ , for  $v = z-1$ ,  $z > 2$  are the right and left boundaries for  $v$  sub-divisions respectively. The  $z \rightarrow \infty$  limit branch can be approximated with

$$\lim_{z \rightarrow \infty} (z, w, 1) \simeq (1, w, 0), \quad (25)$$

and is the right boundary for  $z$  sub-division. This limit branch acts as a separator between different  $w$  sub-divisions since it is impossible for any  $(z, w, v)$  branches to cross over to its left and likewise for the  $(z, w+1, v)$  ones to cross over to its right. By (25), the infinite  $z$  limit recover the  $(1, 0, 0)$  Keplerian orbits in agreement with the non-relativistic limit.

### 3 Roots configuration and analytical solutions

We will first explain the significance of the  $P(u)$  polynomial and how its root configuration constitute periodic orbits. To rephrase our earlier statement about the roots disposition [39], a geometrical bound orbit is defined by a closed domain in  $P(u)$  where values between two distinct positive real roots contain the set of all possible radial distance in that orbit. Within this context, a periodic orbit radial motion can be translated as the particle's initial  $u$ -value starting from one of the root and then oscillate to and fro between the other root of the same domain.

No oscillations occur when the domain have a root that is zero or negative. This correspond to the unbound<sup>3</sup> escaping orbits. We can interpret it as the  $u$ -value coming from negative infinity approaching the positive periastron root, then bounce off this root before going back to the same direction it came from. Circular orbits roots  $u_c$  are *degenerate*, meaning the root value is repeated at least once and thus reduce the total number of distinct roots. These points are illustrated by  $P(u)$  plots in Fig.5. The periastron root always lie to the right of the apastron's one since  $u_p > u_a$ . As  $e \rightarrow 0$ , the gap between roots of a domain shrink and eventually coalesce at  $u_c$  value. We further extend the periodic orbit notation as  $(z, w, v; e)_{outer/inner}$  to indicate the region outside a naked singularity where the periodic orbit reside.

Since the polynomial for RN spacetime is quartic, there are up to two domains corresponding to bound orbits which further solidify the possibility of a periodic orbit pair. Referencing previous works [39, 45, 46], the smaller value domain correspond to orbits of the first kind, the relativistic analogue of Keplerian orbits whilst the larger

---

<sup>3</sup>Another type of unbound trajectory is the plunging orbit, an irreversible journey into the central singularity. In  $P(u)$  context, the  $u$ -value make a 'one-way trip' from the periastron root to positive infinity. This is not possible for RN as radial polynomials with even number terms always exhibit an infinite potential barrier in  $V_{\text{eff}}$  that prevent anything from reaching the singularity.

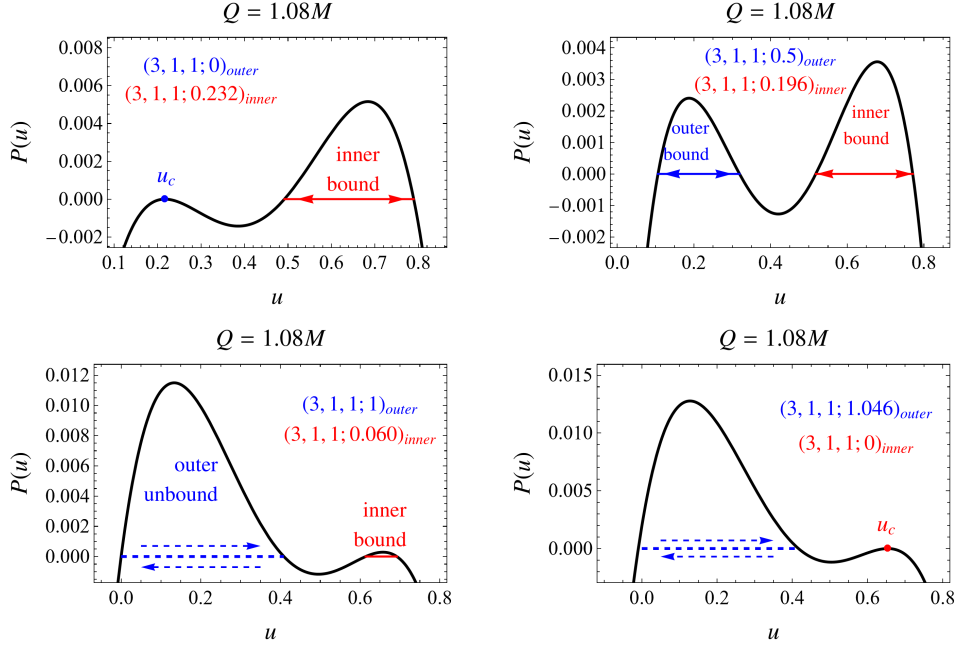


**Fig. 5** Evolution of  $P(u)$  moving upwards along the slope of the  $Q = 1.08M$ ,  $(3, 1, 1)$ -branch, from the emanation point of the outer orbit up to that of the inner orbit. Each plots correspond to values of (9c), (26), (27) and (28). Dashed lines represent the ‘one-way’ motion of unbound escaping orbits.

value domain correspond to orbits of the second kind, a purely relativistic effect. This feature is also present in RN black holes, but it have a more complex global causal structure where the Killing vector fields in the region between the two horizons,  $r_- < r < r_+$  switch causality. On top of that, we need to maximally extend the manifold at both horizons in order to describe a complete geodesic [47]. We will not pursue this case further. Solutions of unbound trajectories will not be presented but readers can find it in [45].

### 3.1 Four real roots

We start by analysing the  $Q = 1.08M$ ,  $(3, 1, 1)$  orbit. We determine  $\lambda$  unique to some  $e$  from Eq.(24) and then plug these into Eqs.(12) to obtain the numerical value of all four roots  $a, b, c, d$  as follows;

$$e = 0, \quad \lambda = 4.6133M, \quad a = 0.78938, \quad b = 0.49177, \quad c = d = 0.21677, \quad (26a)$$

$$e = 0.5, \quad \lambda = 4.7004M, \quad a = 0.77102, \quad b = 0.51816, \quad c = 0.31912, \quad d = 0.10637, \quad (26b)$$

$$e = 1, \quad \lambda = 4.8945M, \quad a = 0.69212, \quad b = 0.61394, \quad c = 0.40862, \quad d = 0 \quad (26c)$$

Observe that a non-zero  $e$  causes all four roots to take real distinct positive values but  $e = 0$  have a value repeated for  $c$  and  $d$ . If we pair up  $a$  with  $b$  and  $c$  with  $d$  and then

inspect the corresponding  $e$  and  $\lambda$  values for each pairing with Eqs.(13), the  $c, d$  pair return the initial value whilst the corresponding  $a, b$  pair output smaller values. The exception to this is the  $c, d$  pair in (26a). Here, the  $a, b$  pair yield a non-zero  $e$ . So, we deduce that if any  $(z, w, v; e)$  sets produce four real roots, then there should be an associative pair of periodic orbits possessing the same  $(L, E)$  values, each residing in different regions surrounding the naked singularity. The corresponding values of  $L$  and  $E$  for each set in (26) where the  $c, d$  pair is blue (left) and  $a, b$  pair is red (right) are;

$$(26a) \Rightarrow L = 2.7394, \quad E = 0.91670, \quad (0, 4.6133M) \Leftrightarrow (0.232, 1.5611M), \quad (27a)$$

$$(26b) \Rightarrow L = 2.8322, \quad E = 0.93440, \quad (0.5, 4.7004M) \Leftrightarrow (0.196, 1.5514M), \quad (27b)$$

$$(26c) \Rightarrow L = 3.1425, \quad E = 1, \quad (1, 4.8945M) \Leftrightarrow (0.0599, 1.5313M) \quad (27c)$$

Clearly, the pairs  $c, d$  and  $a, b$  correspond to the outer and inner region respectively. Then, when we interpolate  $q$ -branch for the outer periodic orbit, values of both  $L$  and  $E$  increase monotonically together with  $e$ . So, the outer  $q$ -branch are straight lines branching upwards diagonally right from the outer stable  $r_c$  segment and end just below the  $E = 1$  line as in Fig.3 and Fig.4. Based on the values in (27), the  $e$  values for the inner region decrease in contrast to increasing  $L$  and  $E$ . So, the inner  $q$ -branch could even extend above the  $E = 1$  line as  $e \rightarrow 0$  and thus emanate from some point on the  $E \geq 1$  portion of the inner stable  $r_c$  segment. The values at the emanation point of the inner  $(3, 1, 1)$  orbit are

$$\begin{aligned} L = 3.1861, \quad E = 1.0098, \quad a = b = 0.65382, \quad c = 0.41637, \quad d = -0.009333 \\ \Rightarrow (1.046, 4.9136M) \Leftrightarrow (0, 1.5295M) \end{aligned} \quad (28)$$

Emanation points of inner periodic orbits cannot originate from  $r_{\gamma-} \leq r_c \leq r_{\gamma+}$ , where time-like circular orbits are forbidden in Case 1. This imply that there is a limited number of inner periodic orbit that could exist for certain  $Q$  and even fewer associative pairs of periodic orbits (Fig.6). Also, any inner  $q$ -branch from the four real roots configuration must specifically emanate from points above  $r_{int}$ , excluding the critical point in Case 2. Thus, the emanation range<sup>4</sup> of an inner periodic orbit  $q$ -branch containing four real roots is  $r_{int; in} < r_c < r_{\gamma-}$  for Case 1 and  $r_{int; in} < r_c < r_{OSCO}$  for Case 2. A small eccentricity range for inner periodic orbits from the emanation point down to the  $e$  value at the  $E = 1$  line have an associated outer escaping orbit. As expected, we find that an inner periodic orbit is always ‘contained’ within its outer counterpart since the apastron of the former do not overlap the periastron of the outer orbit (Fig.7).

To plot periodic orbits, we seek expressions of the radial distance as a function of  $\phi$  in terms of the roots values of  $P(u)$ . So this is where the second usage of elliptic integral comes in. The procedure is to first invert the Jacobi form of the integral,  $\phi(u) = g F(\psi, k)$  to  $u(\phi)$ , then take the reciprocal to get  $r(\phi)$ . When all four roots have

---

<sup>4</sup>This is the range where the middle value solution of Eq.(19) representing the  $e = 0$  limit of inner periodic orbits must take. Obviously, the associated outer periodic orbit correspond to the largest solution.

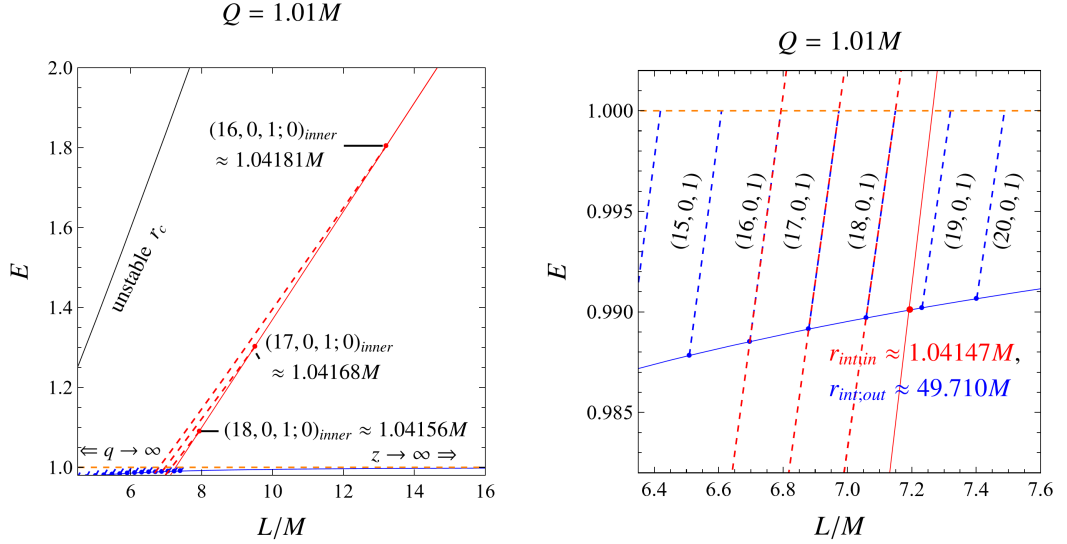


**Fig. 6** Portions of the inner periodic orbits  $q$ -branch with four real roots. An extra significant figure was added to distinguish the emanation points radial values and  $r_{init,in}$ . Right figure:  $q$ -branches of the outer and inner orbits completely overlap one another.

real values (including negative reals), the general form of  $r$  as in 250.04, pg 97 of [43] is

$$r(\phi) = \frac{A_1 + A_2 \operatorname{sn}^2(g^{-1} \phi, k)}{A_3 + A_4 \operatorname{sn}^2(g^{-1} \phi, k)} \quad (29)$$

where  $\operatorname{sn}$  is the Jacobi elliptic sine function and  $A_1, A_2, A_3, A_4$  are functions of roots  $a, b, c, d$ . Arrangement of roots in these functions depends on  $\psi$  which in turn, depend on the initial conditions. Because of our choice of root ordering,  $g^{-1}$  and  $k$  for the general form in (29) will always be (see pg.275 [44]),

$$g^{-1} = \frac{Q}{2} \sqrt{(a-c)(b-d)}, \quad k^2 = \frac{(a-b)(c-d)}{(a-c)(b-d)}, \quad (30)$$

Choosing the initial condition to be at the apastron of each orbit,  $d$  for the outer region and  $b$  for the inner region couple with (30), we have

$$\text{outer: } r(\phi)_{\text{I}} = \frac{(a-c) + (c-d) \operatorname{sn}^2(g^{-1} \phi, k)}{(a-c)d + a(c-d) \operatorname{sn}^2(g^{-1} \phi, k)}, \quad (31a)$$

$$\text{inner: } r(\phi)_{\text{II}} = \frac{(c-a) + (a-b) \operatorname{sn}^2(g^{-1} \phi, k)}{(c-a)b + c(a-b) \operatorname{sn}^2(g^{-1} \phi, k)} \quad (31b)$$

We plot all orbits in Cartesian coordinates  $(r(\phi) \cos \phi, r(\phi) \sin \phi)$ . Orbits in Fig.3 and Fig.7 are plotted with Eqs.(31). We could use analytical solutions expressed with Weierstrass elliptic functions [46] but it require converting the radial polynomial from



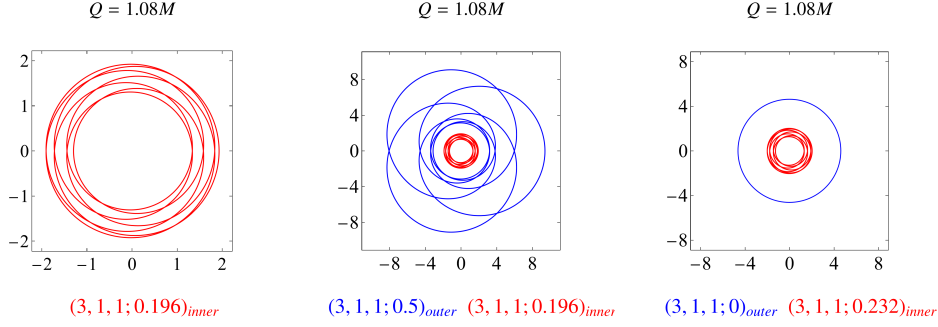


**Fig. 7** Plots of the associative pair of  $Q = 1.08M$ ,  $(3, 1, 1)$  orbits. Both orbits in the middle and right figures possess the exact same  $L$  and  $E$  values.

quartic to cubic. We will just stick to the Jacobi version as it allow a more intuitive visual representation of  $P(u)$  plots.

### 3.2 Two real and two complex roots

If we now increase the eccentricity of an inner periodic orbit and extend the  $q$ -branch below the outer stable circular orbits segment, the values of  $a$  and  $b$  turn complex and are conjugates of each other. The shape of the inner  $q$ -branch starts to curve and reach an energy minima at some moderate eccentricity, roughly  $0.1 \lesssim e \lesssim 0.5$ , before extending upwards left of the minima and terminate at  $E = 1$ . A rule of thumb is that a larger  $q$  generates larger  $e$  corresponding to the minimum  $E$ . This means that it is now possible for two different eccentricities of a single inner orbit set to possess the same  $E$  value (Fig.8). Like the outer  $q$ -branches [37], it is not possible for neighbouring inner  $q$ -branches to cross or intersect one another.

All other outer and inner periodic orbits that emanate from  $r_c > r_{int;out}$  and  $r_* < r_c < r_{int;in}$  respectively also display this root configuration. The  $q$ -branch shape for each respective regions is the same as described previously except for inner  $q$ -branches that emanate from points closer to  $r_*$ . These particular branches resemble half of a parabola with  $e = 0$  being the minimum point and increasing  $e$  always extend the branches upwards. Hence,  $E$  values increase monotonically with  $e$  but  $L$  values not necessarily so as the branch may start swerving towards the right, usually around the half way mark,  $e \gtrsim 0.5$  (Fig.15). Most of Case 3  $q$ -branches take this shape but could only emanate from the left side <sup>5</sup> of the circular orbits curve (Fig.16). The energetically unbound region to the left and right of the top part of both stable  $r_c$  segments also contain two complex roots (Fig.8). This can be surveyed by calculating the root values (12) from any arbitrary points from those regions.

Eqs.(31) could not be used when complex value roots are present. Instead, we need the form given in 250.05, pg 97 of [43],

$$r(\phi)_{III} = \frac{\alpha_1 + \alpha_2 \operatorname{cn}(g^{-1}\phi, k)}{\alpha_3 + \alpha_4 \operatorname{cn}(g^{-1}\phi, k)}, \quad (32)$$

<sup>5</sup>Emanation points are smallest solutions of Eq.(19).

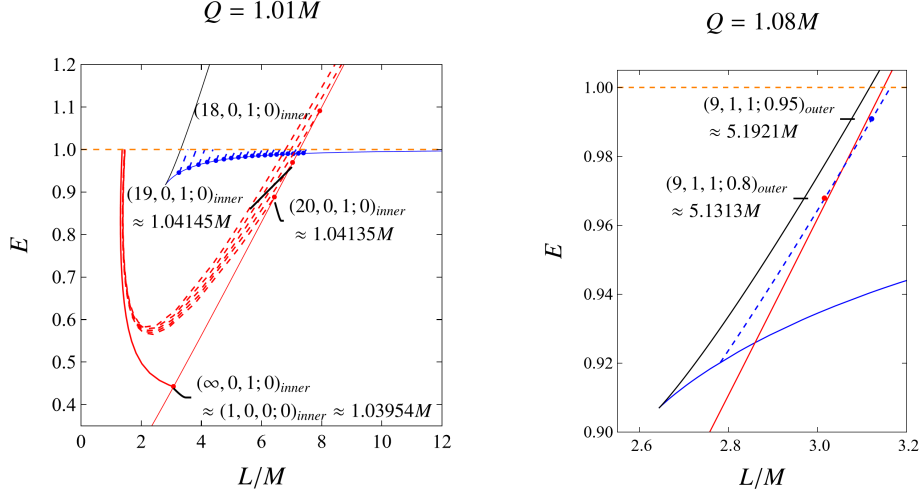


**Fig. 8** Left figure: The limit branch for the inner Keplerian orbit is the solid red half parabola shape curve. Right figure: This outer  $q$ -branch resides in domains with four real roots at  $0 < e \leq 0.864$  and two complex roots at  $0.864 < e < 1$ .

where  $\text{cn}$  is the Jacobi elliptic cosine function and the functions  $\alpha_1, \alpha_2, \alpha_3, \alpha_4$  are all dependant on the roots values but  $\alpha$ -values must be real. Eq.(32) work exactly the same way for both regions if we define the initial condition to start at the apastron like before. In this case, we shall relabel the roots  $c, d$  to  $u_p, u_a$  and  $a, b$  to  $z, \bar{z}$ . The rest of the parameters for this configuration are given by 259.00, pg. 133 of [43]:

$$\begin{aligned} a_1^2 &= -\frac{(z - \bar{z})^2}{4}, & b_1 &= \frac{z + \bar{z}}{2}, \\ A^2 &= (u_p - b_1)^2 + a_1^2, & B^2 &= (u_a - b_1)^2 + a_1^2, \\ g &= \frac{1}{Q\sqrt{AB}}, & k^2 &= \frac{(u_p - u_a)^2 - (A - B)^2}{4AB}, \end{aligned}$$

Or we could express them, including  $\alpha$ , explicitly involving all four roots  $u_p, u_a, z, \bar{z}$ ,

$$\alpha_{1,2} = A \pm B = \sqrt{(u_p - z)(u_p - \bar{z})} \pm \sqrt{(u_a - z)(u_a - \bar{z})}, \quad (33)$$

$$\alpha_{3,4} = Au_a \pm u_p B = u_a \sqrt{(u_p - z)(u_p - \bar{z})} \pm u_p \sqrt{(u_a - z)(u_a - \bar{z})}, \quad (34)$$

$$g^{-1} = Q\sqrt{AB} = Q\sqrt{\sqrt{(u_p - z)(u_p - \bar{z})}\sqrt{(u_a - z)(u_a - \bar{z})}}, \quad (35)$$

$$k^2 = \frac{1}{4} \left( 2 + \frac{u_p(z + \bar{z} - 2u_a) + u_a(z - \bar{z}) - 2z\bar{z}}{\sqrt{(u_p - z)(u_p - \bar{z})}\sqrt{(u_a - z)(u_a - \bar{z})}} \right) \quad (36)$$

Plots of periodic orbits with Eqs.(33-36) are shown in Fig.9. Obtaining a sensible real  $\lambda$  via (24) is done by first considering the  $e = 0$  points along the allowed emanation

range  $r_c > r_{int;out}$  or  $r_* < r_c < r_{int;in}$ . For inner periodic orbits, the lower limit of  $\lambda$  would be the emanation point of the inner  $(\infty, 0, 1)$  limit branch. Then, seek the closest monotonically increasing  $\lambda$  values for  $e > 0$  as before.

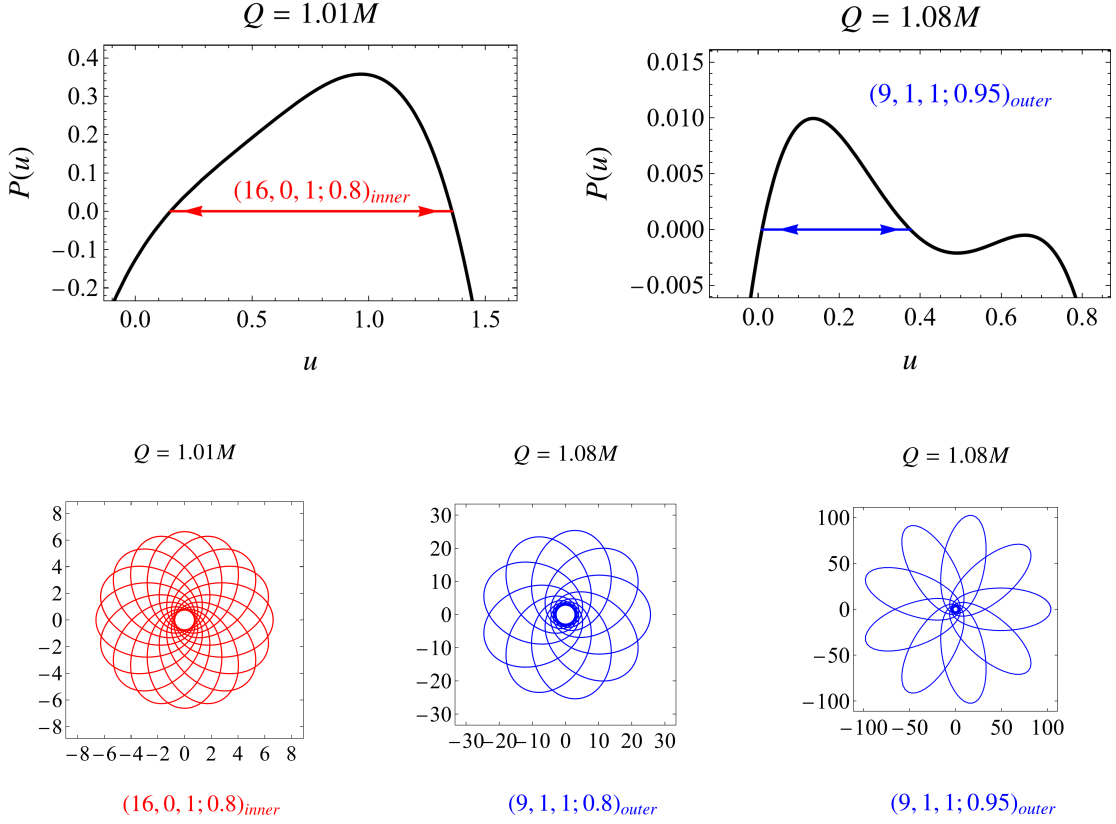


**Fig. 9** Top row:  $P(u)$  plots for  $q$ -branches that typically emanate from  $r_c > r_{int;out}$  or  $r_* < r_c < r_{int;in}$ . Bottom row: The middle and right orbits are based of the two points of the  $q$ -branch in Fig.8. They should be plotted with Eq.(31a) and Eq.(33) accordingly.

### 3.3 Special cases of degenerate roots

Here, we will mention some intriguing parts on the circular orbits curve with degenerate real roots and reveal some striking properties. On any point on the unstable circular orbits segment, we encounter another case of non-oscillatory motion within domains of  $P(u)$ . This happen for the infinite-whirl limit homoclinic orbit [10, 13, 37]. In physical space, this orbit occur when the trajectory start from some arbitrary location before asymptotically approach the radius of an unstable circular orbit. It then remained as a circular orbit for an infinite time unless it is perturbed. In the naked singularity background and with  $P(u)$  being quartic, there exist a pair of homoclinic

orbits for a single  $r_c$  (Fig.10). In  $P(u)$  plots, we view it as the  $u$ -value making a ‘one-way’ trip from either the periastron or apastron root to the degenerate root  $u_c$ , which is now the middle value in the order:  $a > u_c = b = c > d$  (Fig.10).

Studies on analytical solutions for the homoclinic orbits in axially-symmetric space-times can be found in [13, 48]. For spherically-symmetric case, we can easily plot the outer homoclinic orbits via Eq.(31a) by inserting the roots  $a, u_c, d$ . However, we need a different initial condition to plot the homoclinic orbits arising from the inner region. This will be 257.00, pg.124 [43]. It describes trajectory that starts from the periastron,

$$\text{giving } \psi = \arcsin \sqrt{\frac{(b-d)(a-u)}{(a-b)(u-d)}}.$$

Together with  $g^{-1}$  and  $k$  (30), we have

$$r(\phi)_{\text{IV}} = \frac{(b-d) + (a-b) \operatorname{sn}^2(g^{-1} \phi, k)}{(b-d)a + d(a-b) \operatorname{sn}^2(g^{-1} \phi, k)} \quad (37)$$

For Schwarzschild black holes [37, 39], perturbing an unstable circular orbit causes the resulting trajectory to become either an escaping orbit or a plunging orbit based on the direction of perturbation. This is since the closed domain in  $P(u)$  describing bound orbits cease to exist whenever two roots coalesce. However, for RN spacetime, we still observe closed domains in  $P(u)$  plots for the entire unstable circular orbits segment (Fig.10). This suggests that the oscillatory motion could reoccur if the middle  $u_c$  root is perturbed towards the direction of another non-negative real root, in other words, the emerging trajectory of particles will remained bound geometrically. This is indeed the case and in fact, it exhibit chaotic motion [14, 49]. Trajectories that arised from perturbations start in a similiar fashion at small  $\Delta\phi$  ( $\approx 15\pi$  in Fig.11) before evolving in radically different manner as  $\Delta\phi$  increases.

Eq.(31b) can be applied to motions caused by inward perturbation but for outward perturbation, we require a different expression and not Eq.(31a). This is the condition in 253.00, pg.107 [43] that describes trajectories starting from the periastron. Then,

we have  $\psi = \arcsin \sqrt{\frac{(b-d)(c-u)}{(c-d)(b-u)}}$  and with (30),

$$r(\phi)_{\text{V}} = \frac{(d-b) + (c-d) \operatorname{sn}^2(g^{-1} \phi, k)}{(d-b)c + b(c-d) \operatorname{sn}^2(g^{-1} \phi, k)} \quad (38)$$

At the critical points in all of Case 1 and 2 naked singularities and also black holes, another root,  $b$  coalesce with  $u_c$  at the ISCO. Moreover, root  $a$  coalesces with  $u_c$  at the OSCO of Case 2. Hence, the critical points contain a triply degenerate root, leaving only two distinct root values overall and a single closed domain in  $P(u)$ . The solution for homoclinic orbits at these critical points cannot take the general form (29) introduced previously since the threefold repeated root made all  $A_1, A_2, A_3, A_4$  terms vanish. Hence, a  $P(u)$  expression with the degenerate root  $u_c$  factored out is required, as in pg. 95 of [45]. A simple rearrangement gives

$$P(u) = (u - u_c)^3(2M - 3Q^2u_c - Q^2u_c)$$

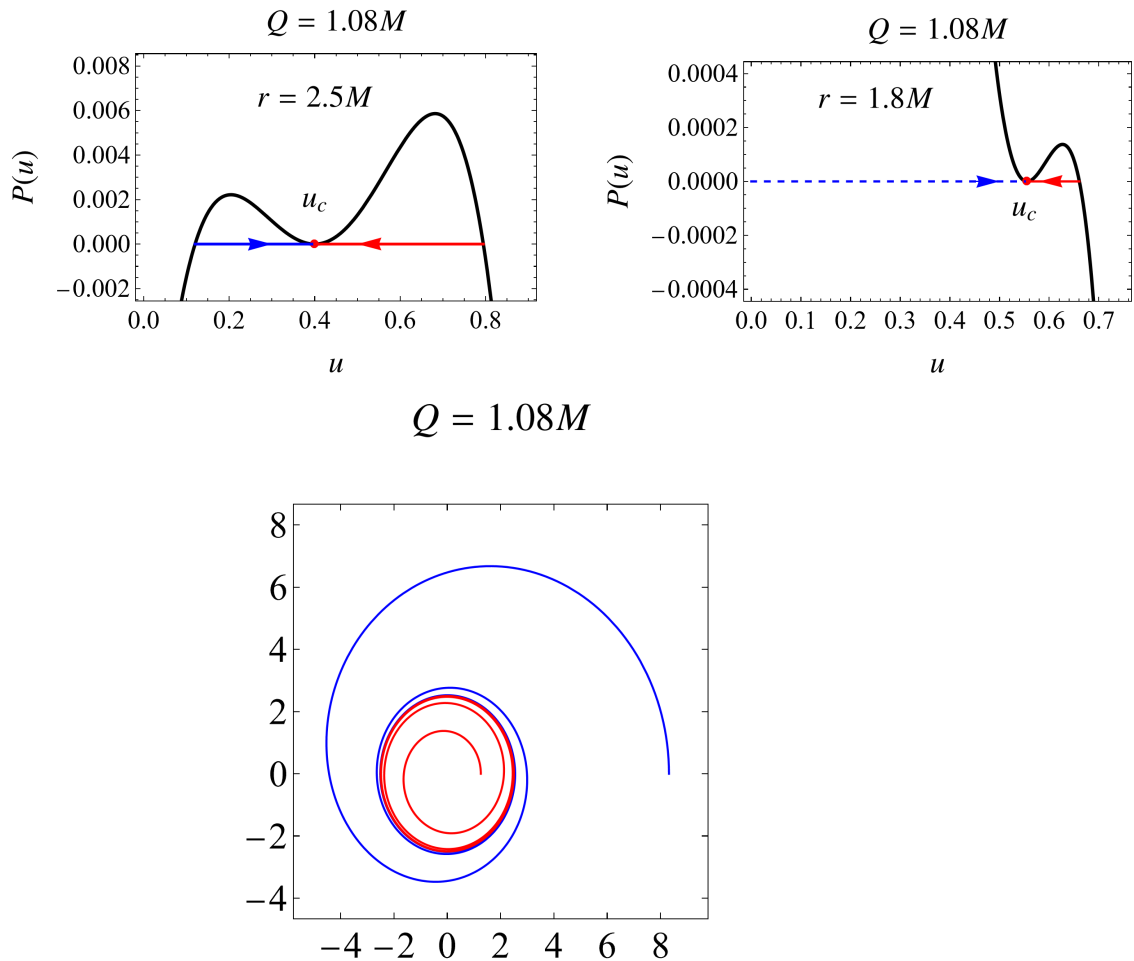


**Fig. 10**  $P(u)$  plots at unstable  $r_c$  values with  $E < 1$  in the top left figure and  $E \geq 1$  in the bottom figure. Top right: The pair of homoclinic orbits at  $r_c = 2.5M$  of  $Q = 1.08M$  plotted with Eqs.(31a) and (37) accordingly.

$$\Rightarrow r(\phi)_{\text{VI}} = \frac{\phi^2 m(Q, u_c)^2 + Q^2}{2m(Q, u_c) + u_c(\phi^2 m(Q, u_c)^2 + Q^2)}, \quad (39a)$$

$$m(Q, u_c) = (M - 2Q^2 u_c) \quad (39b)$$

Fig.12 homoclinic orbits are plotted with Eq.(39). By observing the location of the closed domain of the ISCOs, we deduce that an inner time-like homoclinic orbit asymptotes to  $r_{ISCO}$  and only chaotic motion from inward perturbation is possible. The homoclinic orbit at Case 2A OSCOs is formed by trajectories starting from infinity and asymptote to the null circular orbit radius. Although the sole null circular orbit

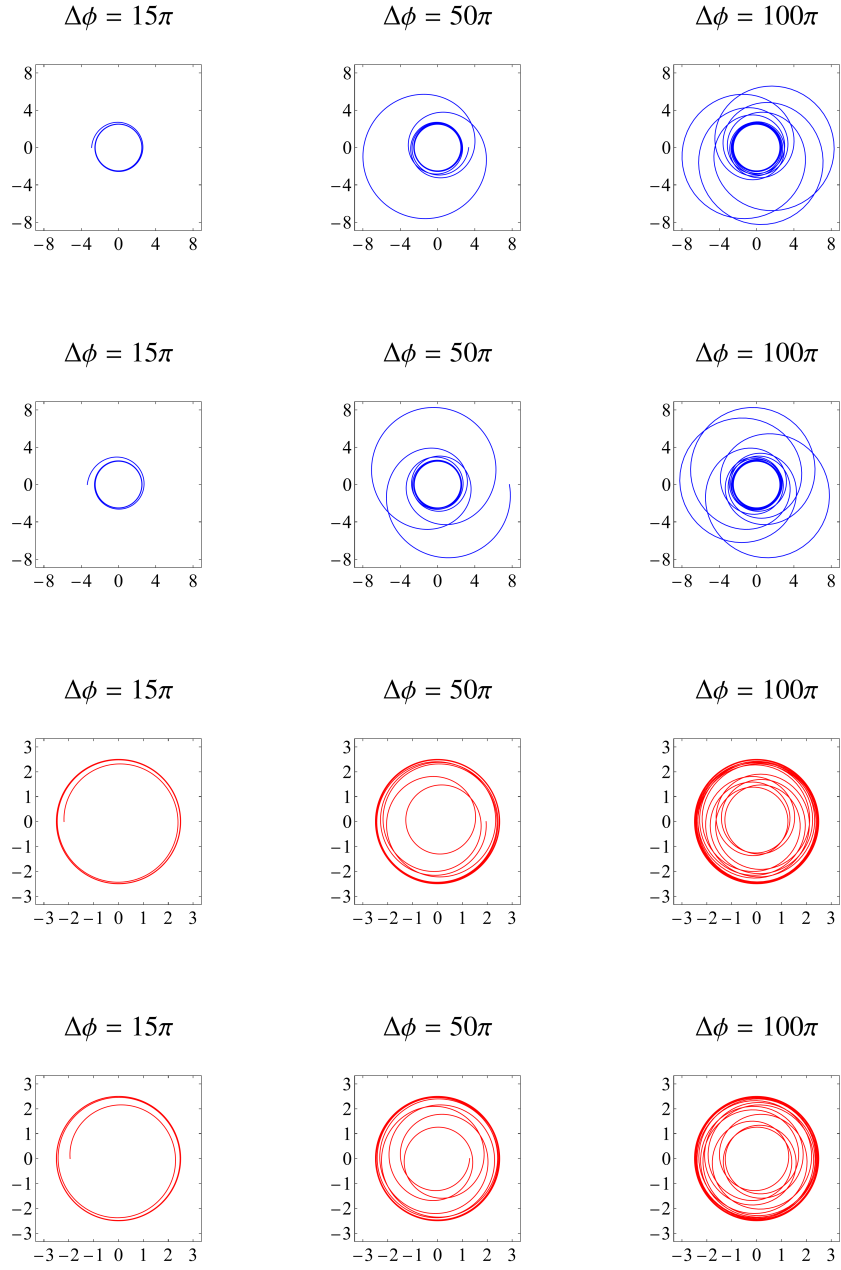


**Fig. 11** The chaotic nature stems from the sensitivity to small perturbations at  $r_c = 2.5M$  of  $Q = 1.08M$ . The blue and red orbits are arise from outward and inward perturbations respectively.

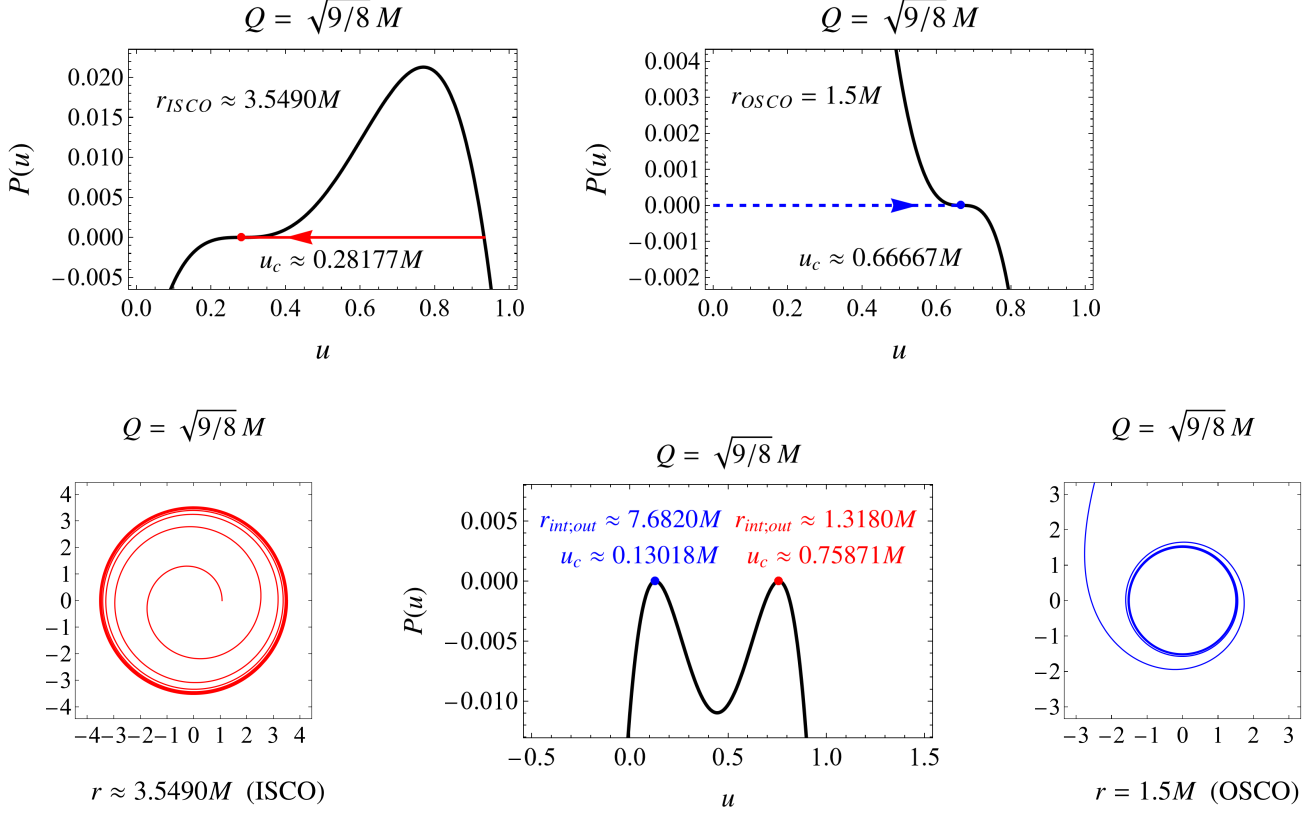


**Fig. 12**  $P(u)$  plots at each critical points of  $Q = \sqrt{9/8}M$  in the top row and the resulting homoclinic orbits in the bottom row. Bottom middle figure shows the  $P(u)$  at the intersection point  $r_{int}$  of the two stable  $r_c$  segments.

at  $r = 1.5M$  for  $Q = \sqrt{9/8}M$  is not strictly a solution to (11), it exhibits a triply degenerate root like every other OSCO of Case 2 and hence can be treated as one. This explains why we consider  $Q = \sqrt{\frac{9}{8}}M$  as part of Case 2.

Finally, we shall briefly mention some trivial  $r_c$  values. At the intersection of the two stable circular orbits segments in  $(L, E)$ -space of Case 1 and 2 (Fig.2), there is a pair of degenerate roots,  $c = d$  and  $a = b$ . So, there could only be a pair of circular orbits, each with radius corresponding to the degenerate roots (Fig.12). At  $r = 2.5M$  of  $Q = \frac{\sqrt{5}}{2}M$  we find the only possible case where all four roots degenerate to the same value,  $a = b = c = d$ , i.e. the point where the two critical points from Case 2 coalesce upon transitioning to Case 3. Both of these types of circular orbits do not change shape when perturbed, thus we can name them as *hyperstable circular orbits*.

The  $P(u)$  roots structure of any  $r_c$  values from  $r_{IUCO} \leq r_c \leq r_{\gamma^-}$  (Case 1) or  $r_{IUCO} \leq r_c \leq r_{OSCO}$  (Case 2A) on the inner stable circular orbits segment clearly indicate an inner circular orbit associated with an unbound outer orbit, but now,

values of both roots for the outer region are smaller than  $u_c$  of the inner region. The periastron value  $c$  of  $r_{IUCO}$  is the smallest possible radial distance away from the singularity where trajectories from the outer region could reach. Therefore, there is always an outer unbound orbit with  $r_{IBCO} \leq r_c \leq r_{IUCO}$  possessing the same  $L$  and  $E$  values with a type of inner bound orbit; either periodic, circular or chaotic, depending on the value of  $r_c$ .

## 4 Generalization of domains and naked singularities $q$ -branch distributions

### 4.1 Domains $\mathcal{D}_k$ where periodic orbits are located in $(L, E)$ -space

Gathering relevant results from the previous sections, we can outline the domains  $\mathcal{D}_k$  in  $(L, E)$ -space where periodic orbits can or cannot be found. As in [37], domains in this section are defined as the sets of  $(L, E)$  values confined within a specific region in the parameter space that give rise to either one or two particular type of orbits.

We first bring up Case 1 and the two variations of Case 2. In Sec. 3.2, we observed that  $(L, E)$  values with four real roots lie in the narrow area confined by the three distinct segments of the  $r_c$  curve representing the two stable regions and the unstable region. This area includes all points that lie exactly on both the stable circular segments of the curve but exclude  $r_{int}$  and the critical points. Therefore, we define  $\mathcal{D}_1$  to be the part of the area lying entirely below the  $E = 1$  line and  $\mathcal{D}_2$  to be the part of the area above and including the  $E = 1$  line.  $\mathcal{D}_1$  is the only region whose  $(L, E)$  values are capable of producing periodic orbit pair of two different size. Furthermore,  $\mathcal{D}_2$  is where we find a pair of an outer escaping orbit and a low eccentricity inner periodic orbit that is remarkably unbound energetically and bound geometrically. Also,  $\mathcal{D}_2$  does not exist for Case 2B since the whole  $r_c$  graph lie entirely below the  $E = 1$  line.

Then in Sec. 3.3, we uncovered areas with two real and two complex roots. We label  $\mathcal{D}_3$  as the area entirely to the right of inner stable  $r_c$  segment, below the  $E = 1$  line, above and including the outer stable  $r_c$  segment.  $\mathcal{D}_4$  will be the area confined to the right of the  $L = 0$  axis, left of both the unstable  $r_c$  segment plus the inner stable  $r_c$  segment, including all points on the latter, and entirely below both the outer stable  $r_c$  segment and the  $E = 1$  line. Again,  $r_{int}$  and critical points are not part of both of these domains. The complex roots prohibit a second bound orbit from forming in both  $\mathcal{D}_3$  and  $\mathcal{D}_4$ . Both of these domains typically contain  $(z, 0, v)$  orbits with large  $z$  and relatively low  $v$ . The entire  $E \geq 1$  region minus both  $\mathcal{D}_2$  and the unstable  $r_c$  segment also have this root configuration. This will be our  $\mathcal{D}_5$ .

Finally, in Case 3, there are definitely at least two complex roots present in the entire parameter space. As such, the domains here are relatively simple to define. Unbound orbits always appear in the  $E \geq 1$  region. So it is also  $\mathcal{D}_5$  defined the same way as the preceding paragraph. Case 3 bound orbits will lie in  $\mathcal{D}_6$ , the entire region confined below  $E = 1$  and above the  $r_c$  curve.  $\mathcal{D}_6$  share a resemblance with black holes graphs, in that there is only a single continuous region describing stable bound orbits. Let  $\mathcal{D}_7$  be the lower right quadrant-like part of the parameter space that yield four



**Table 1** Summary of the essential periodic orbits description for domains  $\mathcal{D}_k$  in  $(L, E)$ -space

Domains	Roots configuration	Orbit types	Periodic orbit solution <sup>8</sup>
$\mathcal{D}_1$	Four real	Outer bound, Inner bound	Outer: $r(\phi)_I$ , Inner: $r(\phi)_{II}$
$\mathcal{D}_2$	Four real including one negative	Outer unbound, Inner bound	Inner: $r(\phi)_{II}$
$\mathcal{D}_3$	Two real and two complex	Only outer bound	$r(\phi)_{III}$
$\mathcal{D}_4$	Two real and two complex	Only inner bound	$r(\phi)_{III}$
$\mathcal{D}_5$	Two real including one negative and two complex	Only unbound	-
$\mathcal{D}_6$	Two real and two complex	One bound	$r(\phi)_{III}$
$\mathcal{D}_7$	Four complex	No orbits possible	-
$\mathcal{D}_8$ ( $E < 1$ ) $r_{ISCO} < r_c < r_{IBCO}$	Three real including one degenerate	Homoclinic orbit pairs, perturb gives chaos bound	Outer homo: $r(\phi)_I$ Inner homo: $r(\phi)_{IV}$ Outer chaos: $r(\phi)_V$ Inner chaos: $r(\phi)_{II}$
$\mathcal{D}_8$ ( $E \geq 1$ ) Case 1: $r_{IBCO} \leq r_c \leq r_{\gamma+}$ Case 2: $r_{IBCO} \leq r_c \leq r_{OSCO}$	Three real including one negative and one degenerate	Outer unbound, Inner homoclinic and chaos	Inner homo: $r(\phi)_{IV}$ Inner chaos: $r(\phi)_{II}$
$\mathcal{D}_8$ (Critical points)	Two real including one triply degenerate	ISCO: Inner homoclinic, OSCO: Outer homoclinic	$r(\phi)_{VI}$

<sup>8</sup>We selected our formulas for  $r(\phi)_{I-V}$  from Ref.[43]. For those preferring Ref.[44], the equivalent formulas can be found in 3.147, pg.275-276. For four reals, they are no. 2,6,7,3 for  $r(\phi)_I, r(\phi)_{II}, r(\phi)_{IV}, r(\phi)_V$  respectively. With complex roots, the alternate form for  $r(\phi)_{III}$  is 3.145, no.2, pg.274.

complex roots in all three cases. This means no orbit possessing  $(L, E)$  values from  $\mathcal{D}_7$  are physically possible. For completeness, we will still list a domain  $\mathcal{D}_8$  where we can find the chaotic orbits from perturbations as shown in Sec. 3.3 since its inception homoclinic orbits was established to fit into the taxonomy.

Table 1 classifies all  $\mathcal{D}_k$  together with choices of analytical solutions of periodic orbits or any bound orbits in general. Fig.13 illustrate  $\mathcal{D}_k$  locations in  $(L, E)$ -space graphically.

## 4.2 General distribution pattern of $q$ -branches for Cases 1,2 and 3

Now that we know the domains in  $(L, E)$ -space to find periodic orbits, we can explore properties of the  $q$ -branch distribution for both regions in each case. Beginning with Case 1 and 2 again, the distribution for the outer region basically follow the same rules as black holes in Sec. 2.3 (Fig.4). The main difference is that now there are two different domains,  $\mathcal{D}_1$  and  $\mathcal{D}_3$  where the outer  $q$ -branch can reside. This situation was highlighted in Fig.8 earlier where we have to use different analytical solutions for

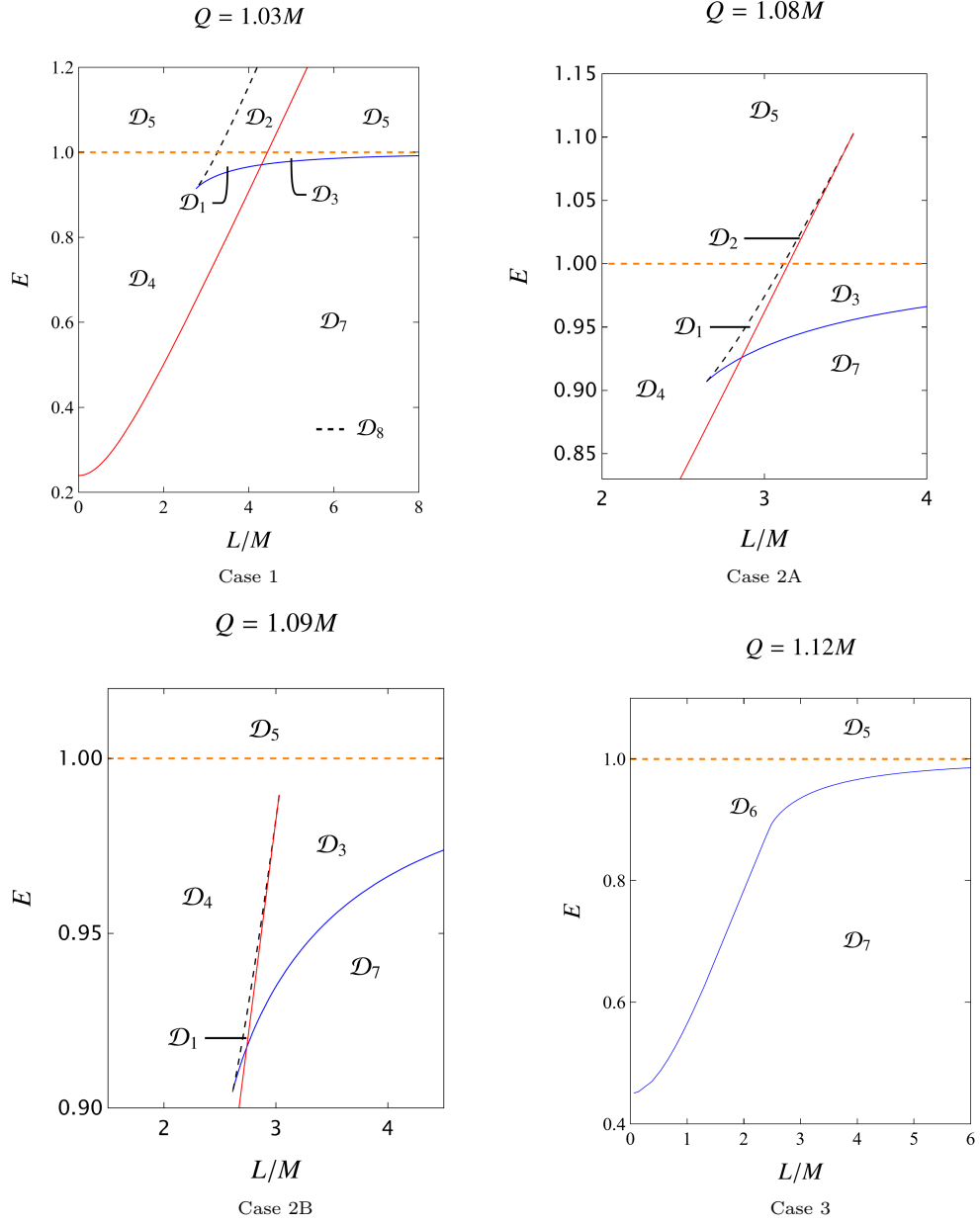


**Fig. 13** The four naked singularity cases and their  $\mathcal{D}_k$  locations in  $(L, E)$ -space. The entire unstable circular orbits segment (dashed black lines) is  $\mathcal{D}_8$ .

each separate  $e$  interval, akin to a piecewise function. On the same note, this type of  $q$ -branch seem to be inherent for all inner orbits  $q$ -branches that emanate from  $\mathcal{D}_2$ . Those cross three separate domains in order from  $\mathcal{D}_2$  to  $\mathcal{D}_1$  to  $\mathcal{D}_4$ .

There are other notable differences of  $q$ -branches for the outer and inner region. One is the difference in direction of emanation for increasing  $w, v$  values, which is equivalent to increasing  $q$  overall since  $q = w + \frac{v}{z}$  [10]. Points of increasing  $q$  goes from right to left for the outer region, whereas for the inner region, it goes upwards along the slope of the inner stable  $r_c$  segment. The infinite  $z$  limit branch for the inner region is visible in a compact  $(L, E)$ -space map. It lie in  $\mathcal{D}_4$  close to the  $L = 0$  axis, acting as the leftmost rational  $q$ -branch for the inner region (Figs.8,14,15). Only quasiperiodic orbits exist to the left of this limit branch.

Strangely, we find a peculiar  $q$ -branch trend when increasing  $q$  values as we get to larger charge  $Q$  from Case 2 onwards. Starting from Case 2A, inner  $q$ -branches with  $w \geq 1$  emanating from some point close to  $r_{int}$  begin to abruptly end at some  $e < 1$  without reaching close to the  $E = 1$  line. Further increasing  $q$  in direction up the slope shrinks the branch more until rationals with large  $w$  (typically  $w \geq 3$ ) super close to the unstable  $r_c$  segment do not emanate anymore branches (Fig.14). A similar trend applies to the outer  $q$ -branch for Case 2B but this time, large  $w$  branch could still appear and those emanating from the stable  $r_c$  segment within  $\mathcal{D}_1$  could not cross the inner stable  $r_c$  segment.

A possible mathematical reasoning we found for this ‘shrinking branch’ trend, especially for  $q$ -branch lying in domains containing complex roots,  $\mathcal{D}_3$  and  $\mathcal{D}_4$ , is that both sides of Eq.(24) yield complex values. For large rationals, after reaching a certain  $e$  value, only complex  $\lambda$  and  $q$  solution remain. In  $(L, E)$ -space, taking some arbitrary points slightly above the tip of the shorter rational  $q$ -branches return an irrational  $q$  value that represent a completely different branch arbitrarily close to the former. However, this does not account for the short rational  $q$ -branches lying in the four real root domain in Case 2B, where the trend seemingly persists into that domain. Physically, it might indicate that periodic orbits with a large number of near-center whirls are harder to form proximately close to both kinds of marginally stable circular orbits (ISCO and OSCO).

Coming to Case 3,  $Q = \frac{\sqrt{5}}{2} M$  is the transition charge between Case 2 and 3. The disappearance of the second stable  $r_c$  segment starting from this  $Q$  cause the  $q$ -branch to distribute in a single region manner. Some distribution properties from Case 2 carry over. For one, this appear to be the last  $Q$  to have an infinite  $w$  limit (at the  $r = 2.5M$  point) and thus homoclinic orbits are not possible in Case 3. The infinite  $z$  limit branch lie towards the left side like the ones for the inner region in Case 1 and 2. Direction of increasing  $q$  is the reverse to that of the outer region, from left to right coupled with the shrinking branch length trend. As such,  $q$ -branches can now only emanate from the left portion of the  $r_c$  curve, particularly from the steep slope (Fig.15).

Increasing  $Q$  further in Case 3 seems to impose a lower limit to the integer value that  $z$  could take. This restricts the number of allowed periodic orbits and thus the range of the  $q$ -branch distribution (Fig.15). Eventually, the exquisite looking small  $q$  value periodic orbits are no longer possible for sufficiently large  $Q$  and what remain are the generic Keplerian and unbound orbits. This may likely be caused by the repulsive ‘anti-gravity’ effect of the naked singularity which increases with  $Q$  [42]. The range of  $E$  values for Case 3  $r_c$  curves shrinks as  $Q \rightarrow \infty$  till the point where we need  $E \simeq 1$  values to maintain bound orbits at really large  $Q$ .

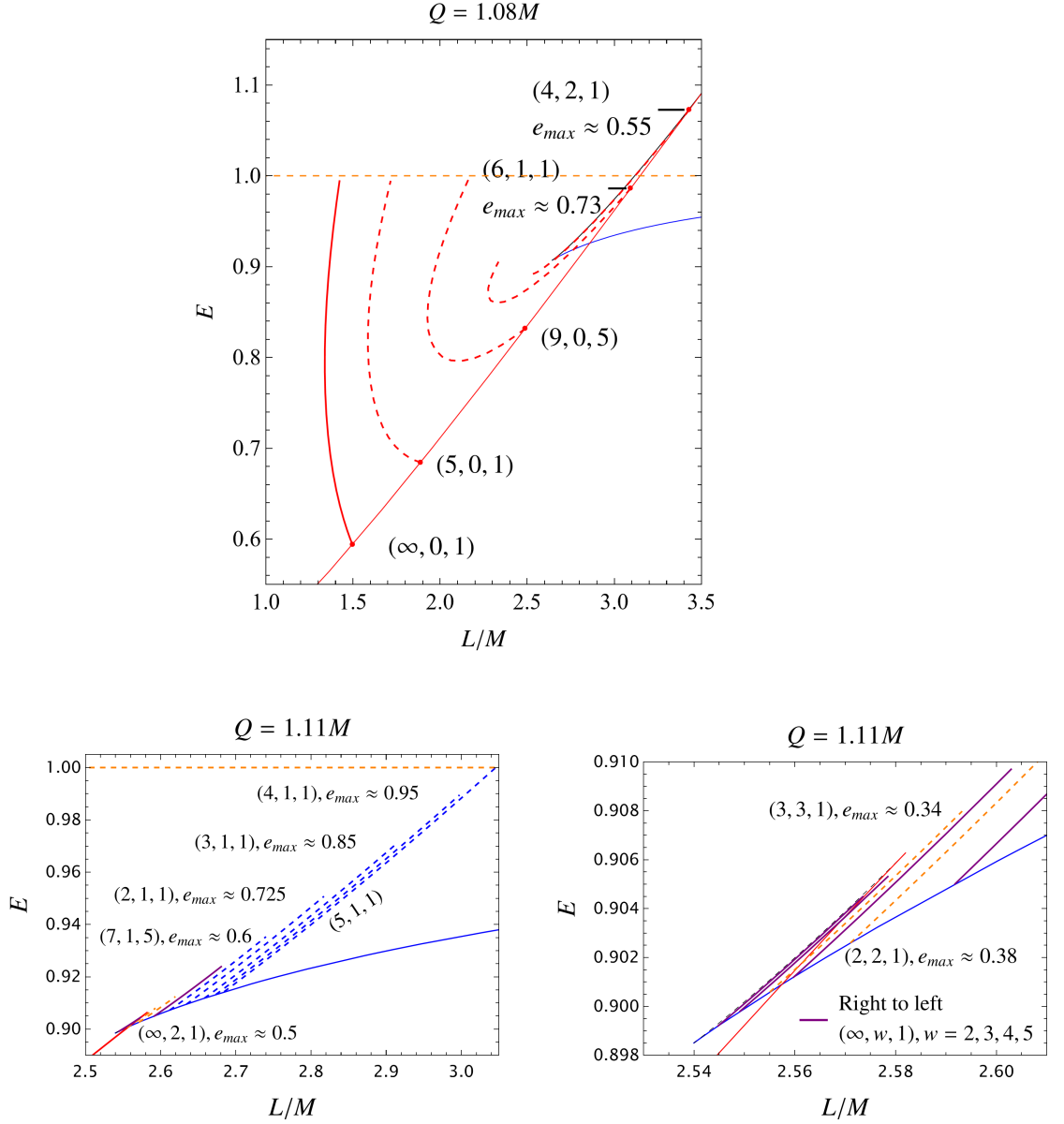


**Fig. 14** The odd trend of  $q$ -branches terminating approximately close to the  $e$  values shown for Case 2.

## 5 Conclusion

In this paper, we have shown how it is possible for time-like neutral test particles to have a pair of periodic orbits with the same  $(z, w, v)$  and  $(L, E)$  values but different

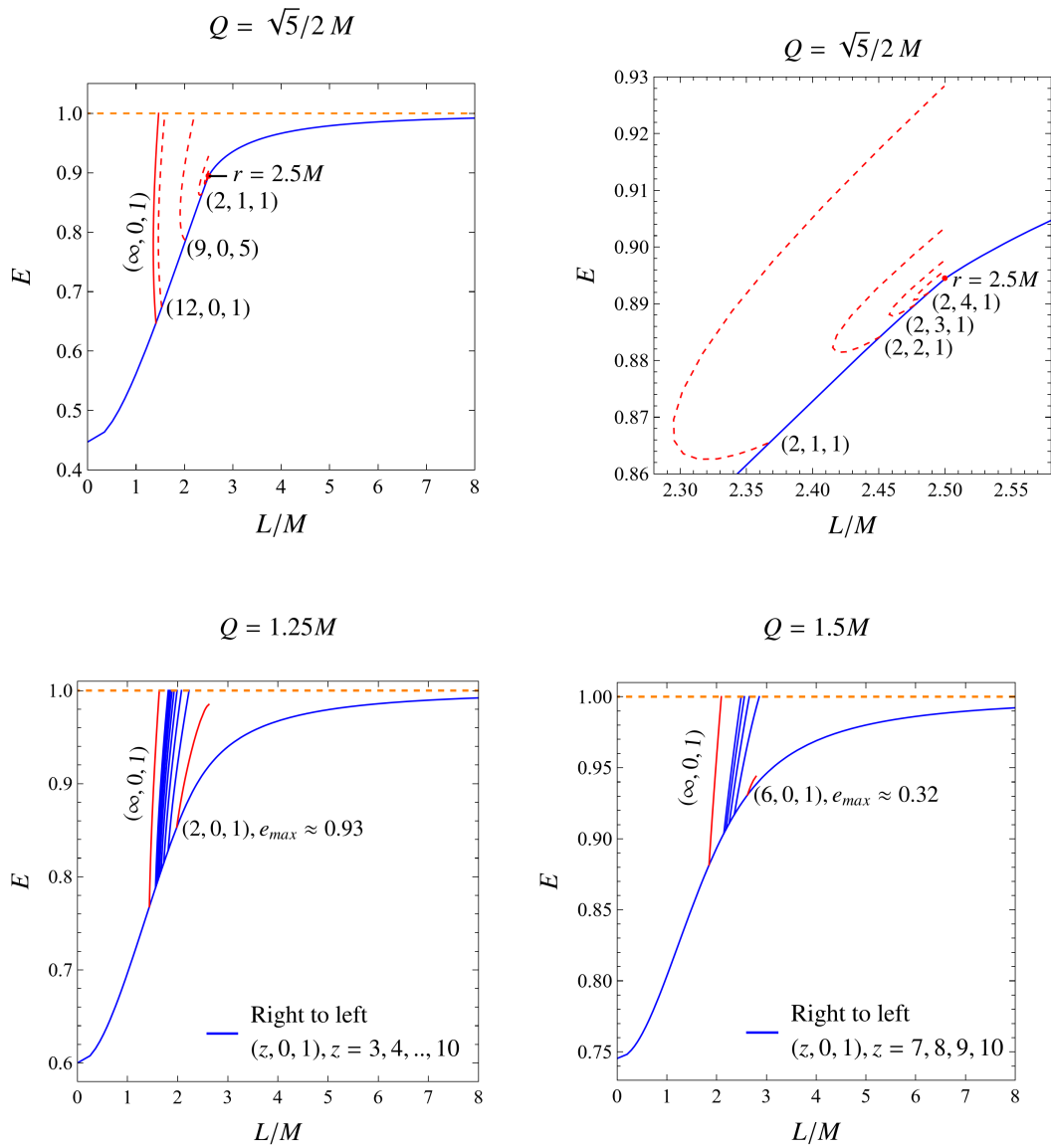


**Fig. 15** The  $q$ -branch distribution for Case 3.

size revolving around a RN naked singularity. We explained the importance of understanding the root configuration of the quartic inverse radial coordinate polynomial  $P(u)$  at different parts in  $(L, E)$  parameter space. The root configuration indicates whether any given  $(L, E)$  values correspond to an associative orbit pair from a possible combination of periodic, circular, homoclinic or unbound. Relatively simple analytical solutions in terms of Jacobi elliptic functions and all four roots of  $P(u)$  are used to

plot the first three aforementioned orbits, providing computational advantages. The solution of homoclinic orbits at the critical points is the exception to this.

We have analysed the three possible scenarios of a RN naked singularity, reasoning which domains in  $(L, E)$ -space could contain physical parameters for periodic orbits. We parametrised several expressions with geometric parameters  $e$  and  $\lambda$ , where these parameters are encoded in  $q$ -branch that emanate from both stable circular orbits segments of the circular orbits curve. We inferred possible physical properties from looking at the different kinds of shape of the branches for each scenarios. We found out how tweaking  $z, w, v$  values change the location of a given  $q$ -branch and then illustrate the general distribution in all scenarios, revealing some novel trends. The analysis and procedures in this paper might be useful for those intending to provide periodic orbit descriptions to other spherically symmetric spacetime or naked singularity background possessing a radial polynomial with degree 4.

The strange trend of decreasing  $q$ -branch length for large rationals in both Case 2 and 3, especially those with  $w \geq 1$  suggest it is harder for periodic orbits with more whirls to zoom out far from its near-circular centre. We had yet to pinpoint whether it is purely a mathematical consequence from the underlying nature of the polynomial roots or there are inherent physical properties in the different regions in naked singularity background that restrict the potential extent of large rationals orbits. In any case, this trend may help in probing the exact size of each region and to constrain the dynamics of non-circular bound orbits surrounding a naked singularity, combined with a more robust mathematical relationship that link rational  $q$  with complex numbers.

## Acknowledgments

Y.-K. L is supported by Xiamen University Malaysia Research Fund (Grant No. XMUMRF/ 2021-C8/IPHY/0001).

## Appendix A: Viète Theorem

Here, we demonstrate how to derive expressions for  $L, E$  and roots  $a, b$  parametrised with  $e$  and  $\lambda$ . We fix the expressions of roots  $c, d = \frac{1 \pm e}{\lambda}$  to conveniently follow Kepler's first law. This means we need to determine the formulas for the two other roots. First, apply Viète theorem [50] to compare the coefficient of terms in (9b) and the arbitrary form of roots  $a, b, c, d$  in (9c). It is written out as,

$$\frac{1 - E^2}{Q^2 L^2} = abcd, \quad (\text{A1})$$

$$\frac{2M}{Q^2 L^2} = abc + abd + acd + bcd, \quad (\text{A2})$$

$$\frac{1}{Q^2} + \frac{1}{L^2} = ab + ac + ad + bc + bd + cd, \quad (\text{A3})$$

$$\frac{2M}{Q^2} = a + b + c + d \quad (\text{A4})$$

In our case,  $cd = \frac{1-e^2}{\lambda^2}$  and  $c+d = \frac{2}{\lambda}$ . Substituting these into (A1) and (A4) gives  $ab = \left(\frac{1-E^2}{Q^2 L^2}\right) \left(\frac{\lambda^2}{1-e^2}\right)$  and  $a+b = \frac{2M}{Q^2} - \frac{2}{\lambda}$  respectively. We recommend deriving  $L$  and  $E$  without finding the explicit expression of  $a$  and  $b$  beforehand. Observe that the RHS of (A2) and (A3) can be factored into  $ab(c+d) + cd(a+b)$  and  $ab + cd + (c+d)(a+b)$  respectively. From here, treat  $ab$ ,  $cd$ ,  $a+b$  and  $c+d$  as variables, do relevant substitutions and then solve (A2) and (A3) simultaneously to obtain the expressions for  $L$  and  $E$  as given in Eqs.(14a).

Then, solving (A1) and (A4) leads to the exact form of roots  $a, b$ . These roots naturally takes the form  $a, b = \frac{A \pm \sqrt{B}}{C}$  where  $A, B, C$  are functions involving  $L, E$  terms. Substituting the  $L, E$  expressions (14a) derived earlier and further simplifications should yield Eqs.(12a). This is why we recommend seeking the  $L, E$  expressions first. In general, this procedure can be use for finding explicit expressions of two quartic roots given the form of the other two roots are fixed.

## Appendix B: Circular Orbits Expressions

Here, we list down some useful circular orbits formulas for naked singularities given in [38] that aid our periodic orbit search. Solving the conditions for critical points,  $V''_{\text{eff}} = 0$  for  $Q > M$  produce three real solutions. These solutions can be expressed in terms of trigonometric functions. In order of increasing magnitude,  $r_1 < r_2 < r_3$ , they are

$$r_1 = 2M - 2\sqrt{4M^2 - 3Q^2} \times \sin \left[ \frac{\pi}{6} + \frac{1}{3} \arccos(B(Q)) \right], \quad (\text{B0})$$

$$r_2 = 2M - 2\sqrt{4M^2 - 3Q^2} \times \sin \left[ \frac{1}{3} \arcsin(B(Q)) \right], \quad (\text{B1})$$

$$r_3 = 2M + 2\sqrt{4M^2 - 3Q^2} \times \cos \left[ \frac{1}{3} \arccos(B(Q)) \right], \quad (\text{B2})$$

$$B(Q) = \frac{8M^4 - 9M^2Q^2 + 2Q^4}{M(4M^2 - 3Q^2)^{3/2}}$$

The smallest solution, (B0) is unphysical as it lie within the  $r_*$  equilibrium sphere and should be ignored. The largest value (B2) represents the ISCO of the outer region surrounding a naked singularity for Cases 1 and 2 and also black holes. (B1) gives the OSCO of the inner region solely for Case 2. Real solutions terminate at Case 3 (except for  $Q = \frac{\sqrt{5}}{2} M$  where  $B1 = B2 = 2.5M$ ) since no critical points exist for this case.

The null circular orbits radii in Case 1 are  $r_{\gamma\pm} = \frac{1}{2} \left( 3M \pm \sqrt{9M^2 - 8Q^2} \right)$  and the minimum radius is simply  $r_* = Q^2/M$ . Time-like circular orbits and hence emanation points for periodic orbits from the inner region cannot exist in the following range;  $r_{\gamma-} \leq r_c \leq r_{\gamma+}$  and  $r_c \leq r_*$ . This is to ensure that the values of  $E$  and  $L$  for time-like particles are well-defined by having the denominator in Eqs.(10) obey  $r_c^2 - 3Mr_c + 2Q^2 > 0$  and the numerator of  $L(r_c, Q)$  obey  $Mr_c - Q^2 > 0$ .

The intersection point  $r_{int}$  of the two stable circular orbits segments in Case 1 and 2 is best solved graphically.

## References

- [1] Reissner, H.: Über die Eigengravitation des elektrischen Feldes nach der Einsteinschen Theorie. *Annalen der Physik* **355**, 106–120 (2006) <https://doi.org/10.1002/andp.19163550905>
- [2] Nordström, G.: On the Energy of the Gravitation field in Einstein's Theory. *Koninklijke Nederlandse Akademie van Wetenschappen Proceedings Series B Physical Sciences* **20**, 1238–1245 (1918)
- [3] M. Zajaček, A.E. A. Tursunov, Britzen, S.: On the charge of the Galactic centre black hole. *Monthly Notices of the Royal Astronomical Society* **480**, 4408–4423 (2018) <https://doi.org/10.1093/mnras/sty2182> [arXiv:1808.07327](https://arxiv.org/abs/1808.07327) [astro-ph.GA]
- [4] Abbott, B.P.e.a.: Observation of Gravitational Waves from a Binary Black Hole Merger. *Phys. Rev. Lett.* **116**, 061102 (2016) <https://doi.org/10.1103/PhysRevLett.116.061102> [arXiv:1602.03837](https://arxiv.org/abs/1602.03837) [gr-qc]
- [5] Benavides-Gallego, C.A., Han, W.-B.: Gravitational Waves and Electromagnetic Radiation from Charged Black Hole Binaries. *Symmetry* **15**(2), 537 (2023) <https://doi.org/10.3390/sym15020537> [arXiv:2209.00874](https://arxiv.org/abs/2209.00874) [gr-qc]
- [6] Event Horizon Telescope Collaboration, K.A.e.a., First M87 Event Horizon Telescope Results. I. The Shadow of the Supermassive Black Hole. *The Astrophysical Journal Letters* **875**(L1) (2019) <https://doi.org/10.3847/2041-8213/ab0ec7> [arXiv:1906.11238](https://arxiv.org/abs/1906.11238) [astro-ph.GA]
- [7] Event Horizon Telescope Collaboration, K.A.e.a.: First Sagittarius A\* Event Horizon Telescope Results. I. The Shadow of the Supermassive Black Hole in the Center of the Milky Way. *The Astrophysical Journal Letters* **930**(L12) (2022) <https://doi.org/10.3847/2041-8213/ac6674> [arXiv:2311.08680](https://arxiv.org/abs/2311.08680) [astro-ph.HE]
- [8] Hsieh, T., Lee, D.-S., Lin, C.-Y.: Strong gravitational lensing by Kerr and Kerr-Newman black holes. *Phys. Rev. D* **103**, 104063 (2021) <https://doi.org/10.1103/PhysRevD.103.104063> [arXiv:2101.09008](https://arxiv.org/abs/2101.09008) [gr-qc]
- [9] Glampedakis, K., Kennefick, D.: Zoom and whirl: Eccentric equatorial orbits around spinning black holes and their evolution under gravitational radiation reaction. *Phys. Rev. D* **66**, 044002 (2002) <https://doi.org/10.1103/PhysRevD.66.044002> [arXiv:gr-qc/0203086](https://arxiv.org/abs/gr-qc/0203086)
- [10] Levin, J., Perez-Giz, G.: A Periodic Table for Black Hole Orbits. *Phys. Rev. D* **77**, 103005 (2008) <https://doi.org/10.1103/PhysRevD.77.103005> [arXiv:0802.0459](https://arxiv.org/abs/0802.0459) [gr-qc]



- [11] Levin, J., Grossman, B.: Dynamics of Black Hole Pairs I: Periodic Tables. *Phys. Rev. D* **79**, 043016 (2009) <https://doi.org/10.1103/PhysRevD.79.043016> [arXiv:0809.3838](https://arxiv.org/abs/0809.3838) [gr-qc]
- [12] Grossman, R., Levin, J.: A Periodic Table for Black Hole Orbits. *Phys. Rev. D* **79**, 043017 (2009) <https://doi.org/10.1103/PhysRevD.79.043017> [arXiv:0811.3798](https://arxiv.org/abs/0811.3798) [gr-qc]
- [13] Levin, J., Perez-Giz, G.: Homoclinic Orbits around Spinning Black Holes. I. Exact Solution for the Kerr Separatrix. *Phys. Rev. D* **79**, 124013 (2009) <https://doi.org/10.1103/PhysRevD.79.124013> [arXiv:0811.3814](https://arxiv.org/abs/0811.3814) [gr-qc]
- [14] Perez-Giz, G., Levin, J.: Homoclinic Orbits around Spinning Black Holes II: The Phase Space Portrait. *Phys. Rev. D* **79**, 124014 (2009) <https://doi.org/10.1103/PhysRevD.79.124014> [arXiv:0811.3815](https://arxiv.org/abs/0811.3815) [gr-qc]
- [15] J. Healy, J.L., Shoemaker, D.: Zoom-Whirl Orbits in Black Hole Binaries. *Phys. Rev. Lett.* **103**, 131101 (2009) <https://doi.org/10.1103/PhysRevLett.103.131101> [arXiv:0907.0671](https://arxiv.org/abs/0907.0671) [gr-qc]
- [16] Levin, J.: Energy Level Diagrams for Black Hole Orbits. *Class. Quant. Grav.* **26**, 35010 (2009) <https://doi.org/10.1088/0264-9381/26/23/235010> [arXiv:0907.5195](https://arxiv.org/abs/0907.5195) [gr-qc]
- [17] V.Misra, Levin, J.: Rational Orbits around Charged Black Holes. *Phys. Rev. D* **82**, 083001 (2010) <https://doi.org/10.1103/PhysRevD.82.083001> [arXiv:1007.2699](https://arxiv.org/abs/1007.2699) [gr-qc]
- [18] R. Grossman, J.L., Perez-Giz, G.: The harmonic structure of generic Kerr orbits. *Phys. Rev. D* **85**, 023012 (2012) <https://doi.org/10.1103/PhysRevD.85.023012> [arXiv:1105.5811](https://arxiv.org/abs/1105.5811) [gr-qc]
- [19] G. Z. Babar, A.Z.B., Lim, Y.-K.: Periodic orbits around a spherically symmetric naked singularity. *Phys. Rev. D* **96**, 084052 (2017) <https://doi.org/10.1103/PhysRevD.96.084052> [arXiv:1710.09581](https://arxiv.org/abs/1710.09581) [gr-qc]
- [20] C. Liu, C.D., Jing, J.: Periodic orbits around Kerr Sen black holes. *Commun. Theor. Phys.* **71**(12 1461) (2019) <https://doi.org/10.1088/0253-6102/71/12/1461> [arXiv:1804.05883](https://arxiv.org/abs/1804.05883) [gr-qc]
- [21] M. Azreg-Aïnou, B.D.M.J.T.Z.Q.W. Z. Chen, Lim, Y.-K.: Orbital mechanics and quasiperiodic oscillation resonances of black holes in Einstein-Æther theory. *Phys. Rev. D* **102**, 044028 (2020) <https://doi.org/10.1103/PhysRevD.102.044028> [arXiv:2004.02602](https://arxiv.org/abs/2004.02602) [gr-qc]
- [22] Zhang, J., Xie, Y.: Probing a black-bounce-Reissner-Nordström spacetime with precessing and periodic motion. *Eur. Phys. J. C* **82**(10 854) (2022) <https://doi.org/10.1140/epjc/s10052-022-0854-0>

[org/10.1140/epjc/s10052-022-10846-4](https://doi.org/10.1140/epjc/s10052-022-10846-4)

- [23] R. Wang, F.G., Chen, H.: Periodic orbits around a static spherically symmetric black hole surrounded by quintessence. *Annals Phys.* **447**(1 169167) (2022) <https://doi.org/10.1016/j.aop.2022.169167>
- [24] Z.-Y. Tu, T.Z., Wang, A.: Periodic orbits and their gravitational wave radiations in a polymer black hole in loop quantum gravity. *Phys. Rev. D* **108**, 024035 (2023) <https://doi.org/10.1103/PhysRevD.108.024035> [arXiv:2304.14160](https://arxiv.org/abs/2304.14160) [gr-qc]
- [25] Deng, X.-M.: Periodic orbits around brane-world black holes. *Eur. Phys. J. C* **80**(6 489) (2020) <https://doi.org/10.1140/epjc/s10052-020-8067-7>
- [26] Deng, X.-M.: Geodesics and periodic orbits around quantum-corrected black holes. *Phys. Dark Univ.* **30**(100629) (2020) <https://doi.org/10.1016/j.dark.2020.100629>
- [27] Lin, H.-Y., Deng, X.-M.: Bound Orbits and Epicyclic Motions around Renormalization Group Improved Schwarzschild Black Holes. *Universe* **8**(5 278) (2022) <https://doi.org/10.3390/universe8050278>
- [28] Y.-Z. Li, X.-M.K.: Precessing and periodic timelike orbits and their potential applications in Einsteinian cubic gravity. *The European Physical Journal C* **84**(5 529) (2024) <https://doi.org/10.1140/epjc/s10052-024-12895-3> [arXiv:2401.16071](https://arxiv.org/abs/2401.16071) [gr-qc]
- [29] Penrose, R.: Gravitational Collapse: The Role of General Relativity. *Riv. Nuovo Cim* **1**, 252–276 (1969)
- [30] M. Patil, M.K. P. S. Joshi, Nakao, K.: Acceleration of particles and shells by Reissner-Nordström naked singularities. *Phys. Rev. D* **86**, 084023 (2012) <https://doi.org/10.1103/PhysRevD.86.084023> [arXiv:1108.0288](https://arxiv.org/abs/1108.0288) [gr-qc]
- [31] R. S. S. Vieira, W.K.Z.S. J. Schee, Abramowicz, M.: Circular geodesics of naked singularities in the Kehagias-Sfetsos metric of Hořava’s gravity. *Phys. Rev. D* **90**, 024035 (2014) <https://doi.org/10.1103/PhysRevD.90.024035> [arXiv:1311.5820](https://arxiv.org/abs/1311.5820) [gr-qc]
- [32] Vieira, R.S.S., Kluźniak, W.: Astrophysical cloaking of a naked singularity. *Monthly Notices of the Royal Astronomical Society* **523**, 4615–4623 (2023) <https://doi.org/10.1093/mnras/stad1718> [arXiv:2304.05932](https://arxiv.org/abs/2304.05932) [astro-ph.HE]
- [33] Mishra, R., Kluźniak, W.: Equilibrium tori orbiting Reissner-Nordström naked singularities. *Proceedings of RAGtime (23-25)*, 151–166 (2023) [arXiv:2312.01827](https://arxiv.org/abs/2312.01827) [gr-qc]
- [34] R. Shaikh, R.N.P.S.J. P. Kocherlakota: Shadows of spherically symmetric black

- holes and naked singularities. *Monthly Notices of the Royal Astronomical Society* **482**, 52–64 (2019) <https://doi.org/10.1093/mnras/sty2624> arXiv:1802.08060 [astro-ph.HE]
- [35] C. Chakraborty, S.B.: Near- and sub-solar-mass naked singularities and black holes from transmutation of white dwarfss arXiv:2401.08462 [astro-ph.HE]
- [36] P. S. Joshi, S.B.: Primordial naked singularities arXiv:2401.14431 [gr-qc]
- [37] Lim, Y.-K., Yeo, Z.-C.: Energies and angular momenta of periodic Schwarzschild geodesics. *Phys. Rev. D* **109**, 024037 (2024) <https://doi.org/10.1103/PhysRevD.109.024037> arXiv:2401.13894 [gr-qc]
- [38] D. Pugliese, H.Q., Ruffini, R.: Circular motion of neutral test particles in Reissner-Nordström spacetime. *Phys. Rev. D* **83**, 024021 (2011) <https://doi.org/10.1103/PhysRevD.83.024021> arXiv:1012.5411 [astro-ph.HE]
- [39] Chandrasekhar, S.: *The Mathematical Theory of Black Holes*. The international series of monographs on physics. Oxford University Press, Chicago (1983)
- [40] Schroven, K., Grunau, S.: Innermost stable circular orbit of charged particles in Reissner-Nordström, Kerr-Newman, and Kerr-Sen spacetimes. *Phys. Rev. D* **103**, 024016 (2021) <https://doi.org/10.1103/PhysRevD.103.024016> arXiv:2007.08823 [gr-qc]
- [41] Zhang, M., Jiang, J.: Internal structures and circular orbits for test particles. *Phys. Lett. B* **834**, 137476 <https://doi.org/10.1016/j.physletb.2022.137476> (2022)
- [42] Cohen, J.M., Gautreau, R.: Naked singularities, event horizons, and charged particles. *Phys. Rev. D* **19**(8), 2273–2279 (1979) <https://doi.org/10.1103/PhysRevD.19.2273>
- [43] Bryd, P.F., Friedman, M.D.: *Handbook of Elliptic Integrals for Engineers and Scientists*. Grundlehren der mathematischen Wissenschaften. Springer, Heidelberg (1971)
- [44] Gradshteyn, I.S., Ryzhik, I.M.: *Table of Integrals, Series, and Products*. Elsevier Science, Amsterdam (2002)
- [45] Slezáková, G.: *Geodesic Geometry of Black Holes*. PhD thesis, University of Waikato (2006)
- [46] Grunau, S., Kagramanova, V.: Geodesics of electrically and magnetically charged test particles in the Reissner-Nordström space-time: Analytical solutions. *Phys. Rev. D* **83**, 044009 (2011) <https://doi.org/10.1103/PhysRevD.83.044009> arXiv:1011.5399 [gr-qc]

- [47] Soltani, F.: Global Kruskal-Szekeres coordinates for Reissner-Nordström space-time. *Phys. Rev. D* **108**, 124002 (2023) <https://doi.org/10.1103/PhysRevD.108.124002> [arXiv:2307.11026](https://arxiv.org/abs/2307.11026) [gr-qc]
- [48] Y.-T Li, D.-S.L. C.-Y. Wang, Lin, C.-Y.: Homoclinic orbits in Kerr-Newman black holes. *Phys. Rev. D* **108**, 044010 (2023) <https://doi.org/10.1103/PhysRevD.108.044010> [arXiv:2302.09471](https://arxiv.org/abs/2302.09471) [gr-qc]
- [49] Bombelli, L., Calzetta, E.: Chaos around a black hole. *Class. Quant. Grav.* **9**, 2573–2599 (1992) <https://doi.org/10.1088/0264-9381/9/12/004>
- [50] Weisstein, E.W.: Vieta's Formulas. From *MathWorld*-A Wolfram Web Resource. <https://mathworld.wolfram.com/VietasFormulas.html>. Accessed: 2024-05-13